TO APPEAR IN OCEAN MODELLING 2018, https://doi.org/10.1016/j.ocemod.2018.10.008

ON THE RESONANT HYDROELASTIC BEHAVIOUR OF ICE SHELVES

Theodosios K Papathanasiou[1], Angeliki E Karperaki[2] and Kostas A Belibassakis[2]

[1]Department of Civil and Environmental Engineering, Brunel University London, Uxbridge UB8 3PH, UK
[2]School of Naval Architecture and Marine Engineering, National Technical University of Athens, Zografos, 15773, Greece

ABSTRACT

Rhythmic hydroelastic oscillations of ice shelves are a key mechanism believed to affect several phenomena observed in Polar Regions, such as the disintegration of ice shelves due to ocean wave impact or even the formation of localised distinctive atmospheric waves. The fundamental and lower hydroelastic modes of an ice-shelf/sub-ice-shelf cavity configuration can be studied by coupling shallow water theory and flexure dynamics of a slender, floating, cantilever beam. A crucial aspect of the analysis is the selection of appropriate boundary conditions at the grounding line of the ice shelf and at the freely floating end. The present study aims to determine appropriate and realistic homogeneous boundary conditions for eigenproblems of resonant ice-shelf vibrations. Through the formulation and solution of a wave impact Reflection-Transmission problem, frequencies that maximise specific norms of the ice-shelf response are identified. It is established that homogeneous conditions on the sub-ice-shelf cavity wave potential value, applied at the front of an ice-shelf, produce eigenfrequencies that in general match the norm maximisation frequencies. The methodology is employed for the prediction of characteristic periods of the Ross and Larsen C ice shelves.

Keywords: ice-shelf resonances, hydroelastic interactions, finite elements, Ross Ice Shelf, Larsen C Ice Shelf

TO APPEAR IN OCEAN MODELLING 2018, https://doi.org/10.1016/j.ocemod.2018.10.008

1. INTRODUCTION

The interaction of ocean waves with ice shelves and ice tongues is considered a key mechanism that affects several phenomena observed in Polar Regions. Waves from the open ocean propagate towards the ice shelves through the Marginal Ice Zone (MIZ) and wave energy, eventually reaching the ice shelves, could be responsible for catastrophic large-scale disintegration events, as recently presented and discussed by Massom et al (2018). The energy carried by ocean waves also contributes to the breaking of sea ice (Montiel and Squire 2017), inducing greater lateral melt and more vigorous stirring of the upper ocean from air drag and floe motion (Zhang et al., 2015). The feedback between wave-induced sea ice breakup and melt in polar regions is demonstrated by Roach et al. (2018) using images from drifting buoys. Typically, regional sea ice loss in the MIZ, could result in increased wave energy eventually reaching the ice shelves. The above processes could further result in the rise of sea water level, coastal erosion and acceleration of global warming effects (Thomson et al. 2016). Notably, a new satellite mission (SKIM) has been proposed by Ardhuin et al. (2017) for measuring currents, ice drift and waves providing enhanced quality data worldwide including Arctic and Antarctic marginal seas.

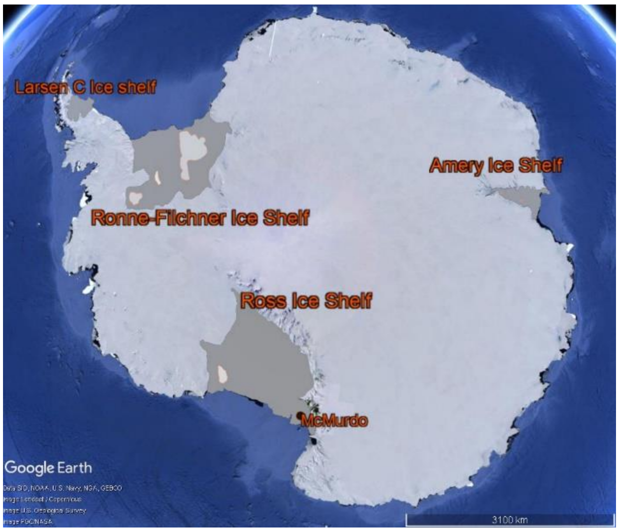

Figure 1. Image of Antarctica, displaying the four largest ice shelves and the location of McMurdo station.

Numerous studies on the stability and disintegration of ice shelves focus on vibrations due to the action of sea swell (Bromirski et al., 2010). This type of periodic, long wave action can induce intense flexural stress fields inside a floating bulk of ice and might thus lead to the expansion of pre-existing rifts (Bromirski et al., 2010; Holdsworth, 1969; Sergienko, 2010; Squire and Williams, 2008; Vinogradov and Holdsworth, 1985). The impact of tsunami and infra-gravity waves has also been identified as a possible source of iceberg calving and potential ice shelf collapse events (Bromirski and Stephen, 2012; Bromirski et al., 2010, 2015, 2017; Brunt et al., 2011). In Brunt et al. (2011), evidence supports the claim that the calving of the Sultzberg Ice Shelf (SIS) in 2011 is triggered by the tsunami generated by the Tohoku earthquake in Japan. Attempts to model the hydroelastic response of ice shelves and ice tongues under long wave excitation have been made by many authors. A dynamic finite element model simulating long wave impact on a floating cantilever representing the SIS has been presented by Papathanasiou et al. (2015).

Vibrations of ice shelves might also be related to the presence of persistent atmospheric waves in the Antarctic region. These localised atmospheric waves, observed at McMurdo (Fig. 1), have periods ranging between 3 to 10 hours (Chen et al., 2016). The origin of such waves might be attributed to the fundamental and low-order modes of the Ross Ice-Shelf resonant vibration, as discussed by Godin and Zabotin (2016). Insight into the complex phenomena of ice shelf resonant, flexural response can be gained from mathematical modelling, accounting for the hydroelastic interactions of ice shelves while retaining a simple form of the governing equations. The large span of ice shelves and ice tongues, along with the non-dispersive nature of very long water waves provide a basis for the development of such models. Indeed, several authors have employed these assumptions and developed models based on the Kirchhoff approximation for thin plates, interacting with long ocean waves (e.g. Godin and Zabotin, 2016; Meylan et al. 2017; Papathanasiou et al. 2015; Sergienko, 2010, 2013, 2017).

An efficient coupled hydroelastic model for the estimation of eigenfrequencies and normal modes of a resonating ice-shelf/sub-ice-shelf cavity system was proposed by Sergienko (2013). Subsequently, Meylan et al. (2017) presented a correction for the complex roots of the characteristic equation in Sergienko's model and reported differences between the former results and the outputs of their proposed scheme. These differences manifest primarily in the first two eigenfrequencies (longer periods) and less in higher-order modes. In both Sergienko (2013) and Meylan et al. (2017) it was assumed that, at resonance conditions, no mass transport occurs through the vertical interface of the ice-shelf and the open sea. This assumption leads to zero velocity or equivalently zero velocity potential gradient at the interface.

On a different front, the analysis of harbour resonances is a problem in the core of coastal engineering and bears similarities with the analysis of ice-shelf resonant vibration modelling. This is because specific boundary conditions have to be applied at the interface between the region of interest (ice shelf or harbour) and the open sea. It is customary in the analysis of harbour resonances to assume that a nodal line exists at the harbour opening. This implies that the upper surface elevation, or equivalently in shallow water theory, the velocity potential is zero on the ficticious line. However, this condition is only approximate and, depending on the geometric characteristics of the harbour, the actual nodal line might be located slightly outside the harbour opening; see Rabonivitch (2009) and the references therein. The purpose of this study is to investigate the effect of this boundary condition at the interface between the ocean and the ice shelf. It is expected that the resulting eigenperiods and eigenmodes will be significantly different than those corresponding to the zero velocity condition (no flux).

Furthermore, this study aims to determine which boundary condition at the interface, zero velocity potential or zero velocity potential gradient is more appropriate. In order to do that, the problem of ice-shelf vibrations, due to long wave impact, will be analysed from a different perspective. In particular, the matching boundary conditions imposing continuity for the velocity potential function and its normal derivative will be applied at the interface between the edge of the ice shelf and the open ocean. These interface conditions have been used by several authors including Papathanasiou et al. (2015), Godin and Zabotin (2016) and Ilyas et al. (2018). The key concepts of the proposed methodology are: **(a)** *apply general interface conditions (instead of boundary conditions) at the ice shelf/ocean interface and analyse ice shelf vibrations as a* Reflection-Transmission problem. That is, to analyse the magnitude of the reflected wave at the ice shelf front and the response generated by the amount of energy actually entering the ice shelf/sub ice shelf cavity region. **(b)** *In this setting, identify frequencies (characteristic frequencies) that maximise certain norms of the response* and **(c)** *compare them with the eigenfrequencies corresponding to different boundary conditions at the sub-ice-shelf cavity/ocean interface*. The present analysis verifies that the use of the zero velocity potential condition at the front of the ice shelf produces much larger eigenperiods. Furthermore it indicates that the zero velocity potential condition is more appropriate (at least for the fundamental and lower resonant modes), as it maximises several norms of the ice shelf response.

The present paper is structured as follows. In Section 2, the governing equations of the ice-shelf/sub-ice-shelf cavity system are presented. Subsequently, in Section 3, the ice shelf hydroelastic vibrations are initially modelled as a wave Reflection-Transmission problem. For the solution of the above problem, the variational formulation of the governing equations is presented and the hydroelastic finite elements developed in Papathanasiou et al. (2014) are employed. The aim is to predict the characteristic periods dictated by the response of the system, and the maximisation of certain response norms. Next, in Section 4 the eigenvalue problems corresponding to each of the homogeneous boundary conditions imposed at the open end of the cavity are considered. In Section 5 the eigenperiods of the numerically solved problems are shown to correspond to either maxima or minima of the Reflection-Transmission problem solution when seen as a function of the forcing wave period. Several cases of large and smaller ice shelves are analysed, including also the Coriolis effects of ice shelves in polar regions. It is demonstrated that the employment of the zero velocity potential condition at the ice-shelf front provides good predictions concerning the characteristic frequencies of the system. Finally in Section 6, the applicability of some simple approximation formulas for the eigenperiods of ice shelves are assessed.

2. GOVERNING EQUATIONS

The present study focuses on the response of ice shelves to long wave forcing and the possibility of long period, resonant vibrations of the ice-shelf/ice-shelf cavity system. A schematic representation of the considered configuration is shown in Fig. 2. To facilitate the analysis, monochromatic waves and uniform conditions along the y axis will be considered. Water waves of large wavelength, compared to the depth of the basin, can be efficiently modelled using the linearised shallow water equations. Thus the equations, governing the evolution of small amplitude, long waves are,

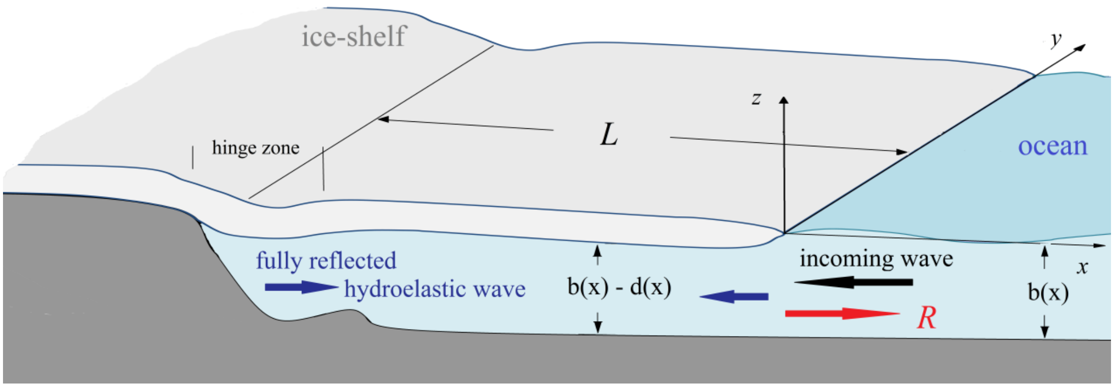

Figure 2. Definition of basic geometry for the ice-shelf/ice-shelf-cavity configuration and wave impact phenomena for the adopted model.

$$\zeta_t + (bu)_x + (bv)_y = 0, \tag{1}$$

$$u_t - fv + g\zeta_x = 0, \tag{2}$$

$$v_t + fu + g\zeta_y = 0, \tag{3}$$

where η, u, v represent the upper surface elevation, the horizontal velocity along the x and y axes respectively. The bathymetry function is denoted by b while f, g denote the Coriolis frequency and the acceleration of gravity respectively.

Assuming uniform conditions along the y direction and employing the velocity potential Ψ, such that $u = \Psi_x$, the three equations reduce to one equation for the velocity potential

$$\Psi_{tt} - (gb\Psi_x)_x + f^2\Psi = 0. \tag{4}$$

The nondimensional variables $\tilde{x} = x/L$, $\tilde{t} = t\sqrt{g/L}$, $\tilde{\Psi} = g^{-1/2}L^{-3/2}\Psi$, are introduced, L being the length of the ice shelf. Using the nondimensional variables and assuming time periodic solutions of the form $\Psi(x)e^{i\omega t}$, Eq. (4) can be written (after dropping tildes) as

$$(B\Psi_x)_x + \left(\Omega^2 - F^2\right)\Psi = 0, \tag{5}$$

where the nondimensional angular frequency $\Omega = \omega\sqrt{L/g}$, and the nondimensional Coriolis frequency $F = f\sqrt{L/g}$, appear. For constant bathymetry B and constant Coriolis frequency F, the general solution of Eq. (5), assuming a wave of unit amplitude propagating towards the ice-shelf is

$$\Psi(x) = \exp\left(i\sqrt{\frac{\Omega^2 - F^2}{B}}x\right) + R\exp\left(-i\sqrt{\frac{\Omega^2 - F^2}{B}}x\right), \tag{6}$$

where R represents the amplitude of the reflected wave by the ice-shelf. Since the incoming wave has amplitude equal to one, R coincides with the reflection coefficient of the system (see also Fig. 2). The above equations are applicable only for frequency Ω above the cut-off frequency *F*, since propagating waves cannot be defined in the water subregion for $\Omega < F$.

The model proposed by Sergienko (2013) will be used for the hydroelastic vibrations of ice shelves. Due to the very large span of ice shelves, compared to their thickness, thin plate models can be employed as a first approximation. The density of ice is denoted as ρ_i and that of water as ρ_w. The deflection of the ice shelf, coinciding with the water elevation inside the cavity region is denoted as $\eta(x)e^{i\Omega t}$, and the velocity potential of the water in the cavity is $\Phi(x)e^{i\Omega t}$. Using the same nondimensional variables as before, the continuity equation for the fluid motion inside the ice-shelf cavity is

$$i\Omega\eta + \left([B - M]\Phi_x\right)_x = 0. \tag{7}$$

where $B = b/L$ and $M = \dfrac{\rho_i h}{\rho_w L}$, h being the ice shelf thickness. In the nondimensional setting adopted, the ice shelf extends from $x = -1$ to $x = 0$. The transition from land to the ocean, that defines the grounding line, takes place in a finite region and is not pointwise (Fricker and Padman, 2006). This region termed the ‘hinge zone’ ranges typically from approximately 1 to 10 km. For ice-shelves with large lengths the transition will be assumed to occur only at point $x = -1$. Away from the hinge zone, the hydrostatic equilibrium (Archimedes principle) produces a depth reduction equal to the draft of the ice shelf $d = \rho_i h / \rho_w$, hence the ice shelf cavity depth in the nondimensional setting becomes $B - M = b/L - d/L$.

The dynamic equation governing the vibrations of the ice shelf reads

$$-\Omega^2 M\eta + \left(K\eta_{xx}\right)_{xx} + \eta + i\Omega\left(1-\left(F/\Omega\right)^2\right)\Phi = 0, \tag{8}$$

and expresses the conservation of linear momentum for the ice shelf. The nondimensional flexural rigidity K that appears in Eq. (8) is defined as $K = \dfrac{Eh^3}{12(1-v^2)\rho_w g L^4}$, where E is Young modulus, and ν Poisson's ratio. The same equation (including the Coriolis effect) has been derived by Sturova (2007) for the study of fluid oscillations in ice-covered, closed basins. The main aim of this work is to determine appropriate simplified conditions at the ice-shelf-cavity/open sea interface able to provide good prediction of the resonant frequencies. As a first step, results are presented and discussed without the effect of the Coriolis acceleration, and thus, $F = 0$ will be considered in the first part of the present analysis. In this specific case the above Eqs.(7) and (8) reduce to the ones already employed for studying ice shelf vibrations by Sergienko (2013) and Meylan et al. (2017). However, the inclusion of Coriolis effects in the model, is expected to produce signifficant changes of the ice-shelf/sub-ice-shelf-cavity system eigenperiods, especially near the polar regions; see Godin and Zabotin (2016, Sec.5). This effect will be further illustrated in Sections 5.2 and 5.3 for specific sites in the Antarctic. Following the works of Sergienko (2013) and Meylan et al. (2017), the ice shelf will be assumed to be clamped at one edge. Furthermore, the bedrock below the ice shelf at $x = -1$ will be assumed impregnable and thus the velocity of the fluid motion will be set to zero at this point. It is thus

$$\eta = 0,\ \eta_x = 0 \text{ and } \Phi_x = 0 \text{ at } x = -1. \tag{9}$$

At the free end of the ice shelf, no bending moment and no shear force conditions imply that

$$\eta_{xx} = 0 \text{ and } \eta_{xxx} = 0, \text{ at } x = 0. \tag{10}$$

It remains to define conditions for the flow velocity at $x = 0$. In the most general setting, interface conditions, expressing conservation of mass and momentum should be applied. For the shallow water model adopted, these can be written as

$$\Phi = \Psi \text{ and } [B - M]\Phi_x = B\Psi_x, \text{ at } x = 0 \tag{11}$$

The above interface conditions are compatible with the formulation of a Reflection-Transmission problem and will be considered in the following section. However, the problem of resonant vibrations can be formulated as an eigenvalue problem as well. In that case, one of the two following conditions needs to be applied instead of Eq. (11): **(i)** the Dirichlet condition $\Phi(0) = 0$ or **(ii)** the Neumann condition $\Phi_x = 0$. These conditions will be considered in Section 4.

REMARK: 1. It is evident that at $x = -1$, a fully reflective boundary is assumed. In more realistic situations, a part of the hydroelastic wave from the ice-shelf/cavity region is expected to be transmitted as a purely flexural wave, considering the ice-shelf/soil as a beam on an elastic foundation. However, the stiffness of the soil is typically very large and the transmitted flexural wave is expected to be of low amplitude.

REMARK 2. The present ideal hydroelastic model is based on the shallow water equations, Eqs. (1-3), in the presence of an elastic floating plate as a termination upper boundary. Extensions of the present model could be considered by coupling it with atmospheric baroclinic model in the upper half space, in conjunction with matching conditions at the floating plate, with application to the study of resonant vibrations of large ice shelves and the induced atmospheric perturbations. The latter are shown to be important, especially concerning the fundamental and low-order resonances of large ice shelves, by Godin and Zabotin (2016). Also, the present system does not account for damping due to dissipation (MacAyeal et al.,2015). These effects in modeling real inhomogeneous ice shelves will be studied in future work.

3. ICE-SHELF RESPONSE AS A REFLECTION-TRANSMISSION PROBLEM

In this section, the resonant vibrations of an ice shelf under the action of long ocean waves will be studied as a Reflection-Transmission problem (Fig. 2). A wave field of the form (6) will be assumed at the open sea region and interface conditions expressing the conservation of mass and momentum will be applied at the interface with the floating ice-shelf. In that manner, the flexural vibrations of the ice-shelf will be studied as a function of the impacting wave characteristics. The solution will be pursued through the discretisation of the variational form of the problem, using high-order finite elements. The variational form for the above system (Eqs. 7-8) with the Coriolis effect is

$$\begin{aligned}&-\Omega^2\int_{-1}^{0} M(x)\bar{v}\eta\, dx+\int_{-1}^{0}K(x)\bar{v}_{xx}\eta_{xx}\,dx+\left[\bar{v}\left(K(x)\eta_{xx}\right)_x\right]_{-1}^{0}-\left[\bar{v}_x K(x)\eta_{xx}\right]_{-1}^{0}+\\&+\int_{-1}^{0}\bar{v}\eta\, dx+i\Omega\left(1-\left(F/\Omega\right)^2\right)\int_{-1}^{0}\bar{v}\Phi\, dx=0,\end{aligned}\tag{12}$$

and

$$i\Omega\int_{-1}^{0}\bar{w}\eta\, dx-\int_{-1}^{0}\left[B(x)-M(x)\right]\bar{w}_x\Phi_x\, dx+\left[\bar{w}\left[B(x)-M(x)\right]\Phi_x\right]_{-1}^{0}=0.\tag{13}$$

where v, w are appropriate weight functions while the overbar denotes the complex conjugate. Using the homogeneous boundary conditions at the grounding line $\eta|_{x=-1}=0$, $\eta_x|_{x=-1}=0$, $\Phi_x|_{x=-1}=0$, the zero bending moment and shear force conditions at the free edge of the ice-shelf $K\eta_{xx}|_{x=0}=0$, $\left(K\eta_{xx}\right)_x|_{x=0}=0$, as well as the interface conditions (11), Eqs. (12) and (13) become

$$-\Omega^2\int_{-1}^{0} M(x)\bar{v}\eta\, dx+\int_{-1}^{0}K(x)\bar{v}_{xx}\eta_{xx}\,dx+\int_{-1}^{0}\bar{v}\eta\, dx+i\Omega\int_{-1}^{0}\bar{v}\Phi\, dx=0\ ,\tag{14}$$

and

$$-i\Omega\int_{-1}^{0}\bar{w}\eta\, dx+\int_{-1}^{0}\left[B(x)-M(x)\right]\bar{w}_x\Phi_x\, dx-\bar{w}(0)B(0)\Psi_x|_{x=0}=0,\tag{15}$$

respectively.

Since $\Psi(0)=R+1$ and $\Psi_x|_{x=0}=i\sqrt{\dfrac{\Omega^2-F^2}{B(0)}}\left(1-R\right)$, testing Eq. (14) with $v=\eta$, and Eq. (15) with $w=\Phi$, and adding we obtain

$$\begin{aligned}&-\Omega^2\left\|\sqrt{M}\eta\right\|_{L^2}^2+\left\|\sqrt{K}\eta_{xx}\right\|_{L^2}^2+\left\|\eta\right\|_{L^2}^2+i\Omega\int_{-1}^{0}\left(\bar{\eta}\Phi-\bar{\Phi}\eta\right)dx+\\&+\left\|\sqrt{B-M}\Phi_x\right\|_{L^2}^2-i\Omega\left(F/\Omega\right)^2\int_{-1}^{0}\bar{\eta}\Phi\, dx=i\sqrt{\Omega^2-F^2}\sqrt{B(0)}\left(1+\bar{R}\right)\left(1-R\right),\end{aligned}\tag{16}$$

where $\|q\|_{L^2}^2 = \int_{-1}^{0} q\bar{q}dx$. Energy conservation and the fact that $x=-1$ is assumed to be a fully reflective boundary, imply that the reflection coefficient has measure equal to one, i.e. $\bar{R}R = |R|^2 = 1$. It is then

$$\begin{aligned}&-\Omega^2\left\|\sqrt{M}\eta\right\|_{L^2}^2 + \left\|\sqrt{K}\eta_{xx}\right\|_{L^2}^2 + \|\eta\|_{L^2}^2 + i\Omega\int_{-1}^{0}\left(\bar{\eta}\Phi - \bar{\Phi}\eta\right)dx + \\ &+\left\|\sqrt{B-M}\Phi_x\right\|_{L^2}^2 - i\Omega\left(F/\Omega\right)^2\int_{-1}^{0}\bar{\eta}\Phi dx = 2\sqrt{\Omega^2-F^2}\sqrt{B(0)}\,\mathrm{Im}(R)\ ,\end{aligned} \tag{17}$$

Using Eq. (7), the Green-Gauss theorem and the interface conditions, it is

$$\begin{aligned}&i\Omega\int_{-1}^{0}\left(\bar{\eta}\Phi - \bar{\Phi}\eta\right)dx = \int_{-1}^{0}\left(\Phi\left([B-M]\bar{\Phi}_x\right)_x + \bar{\Phi}\left([B-M]\Phi_x\right)_x\right)dx = \\ &-2\left\|\sqrt{B-M}\Phi_x\right\|_{L^2}^2 - i\sqrt{\Omega^2-F^2}\sqrt{B(0)}(1-\bar{R})(1+R) + i\sqrt{\Omega^2-F^2}\sqrt{B(0)}(1+\bar{R})(1-R) = \\ &-2\left\|\sqrt{B-M}\Phi_x\right\|_{L^2}^2 + 4\sqrt{B(0)}\sqrt{\Omega^2-F^2}\,\mathrm{Im}(R),\end{aligned}$$

and

$$\begin{aligned}&i\Omega\left(F/\Omega\right)^2\int_{-1}^{0}\bar{\eta}\Phi dx = \\ &\quad -\left(F/\Omega\right)^2\left\|\sqrt{B-M}\Phi_x\right\|_{L^2}^2 - i\left(F/\Omega\right)^2\sqrt{\Omega^2-F^2}\sqrt{B(0)}\left(1+R\right)\left(1-\bar{R}\right) = \\ &\quad -\left(F/\Omega\right)^2\left\|\sqrt{B-M}\Phi_x\right\|_{L^2}^2 + 2\left(F/\Omega\right)^2\sqrt{\Omega^2-F^2}\sqrt{B(0)}\,\mathrm{Im}(R)\ .\end{aligned}$$

Using the above in Eq. (17) the latter becomes (since $\Phi_x = u$):

$$\begin{aligned}&\left\|\sqrt{K}\eta_{xx}\right\|_{L^2}^2 + \|\eta\|_{L^2}^2 - \Omega^2\left\|\sqrt{M}\eta\right\|_{L^2}^2 - \left(1-\left(F/\Omega\right)^2\right)\left\|\sqrt{B-M}u\right\|_{L^2}^2 + \\ &\qquad + 2\Omega\left(1-\left(F/\Omega\right)^2\right)^{3/2}\sqrt{B(0)}\,\mathrm{Im}(R) = 0.\end{aligned} \tag{18}$$

The normed quantities appearing in Eq. (18) define a form of potential-kinetic energy difference in the ice-shelf/ice-shelf cavity system for any given frequency as

$$\Pi(\Omega) = \left\|\sqrt{K}\eta_{xx}\right\|_{L^2}^2 + \|\eta\|_{L^2}^2 - \Omega^2\left\|\sqrt{M}\eta\right\|_{L^2}^2 - \left(1-\left(F/\Omega\right)^2\right)\left\|\sqrt{B-M}u\right\|_{L^2}^2\ . \tag{19}$$

This energy difference is balanced by the term $2\Omega\left(1-\left(F/\Omega\right)^2\right)^{3/2}\sqrt{B(0)}\,\mathrm{Im}(R)$, such that the total energy of the system ice-shelf/ocean is conserved in this model. The above result is examined as a possible indicator of the resonant frequencies of the considered hydroelastic system. It will be shown in the examples presented in Sec.5 that the $\Pi(\Omega)$ zero values agree well with the eigenfrequencies of the ice-shelf/ice-shelf-cavity configuration calculated by using two different types of simplified homogeneous boundary conditions at the cavity-ocean basin interface, namely

$\Phi(0)=0$ or $\Phi_x|_{x=0}=0$. Furthermore, it will be demonstrated that the former Dirichlet condition provides reasonable predictions of the characteristic periods of the system.

The hydroelastic finite element HELFEM(4,5) is employed for the solution of the resulting Reflection-Transmission variational problem (Papathanasiou et al., 2014). Based on the increased degree of interpolation of the above element, the convergence properties of the present numerical scheme are very good. Denoting by $H^k(-1,0;\mathbb{C})$ the space of complex functions with Lebesgue square integrable k^{th} derivative, defined in the interval $(-1,0)$, the variational problem can be formulated as follows:

For each $\Omega\in\mathbb{R}_+$, find $R\in\mathbb{C}$ and $\eta\in\left\{H^2(-1,0;\mathbb{C}):\ \eta(0)=\eta_x(0)=0\right\}$, $\Phi\in H^1(-1,0;\mathbb{C})$ such that for all $v\in V$ and $w\in W$ it is

$$\begin{aligned}&-\Omega^2\int_{-1}^{0}M(x)\bar{v}\eta dx+i\Omega\int_{-1}^{0}\left(\bar{v}\left[1-\left(F/\Omega\right)^2\right]\Phi-\bar{w}\eta\right)dx+\\&+\int_{-1}^{0}K(x)\bar{v}_{xx}\eta_{xx}dx+\int_{-1}^{0}\bar{v}\eta dx+\int_{-1}^{0}\left[B(x)-M(x)\right]\bar{w}_x\Phi_x dx+\\&\qquad+i\sqrt{B(0)}\sqrt{\Omega^2-F^2}R=i\sqrt{B(0)}\sqrt{\Omega^2-F^2}\ ,\end{aligned}\tag{20}$$

and

$$\Phi(0)-R=1.\tag{21}$$

Representing the vector of unknowns inside an element (i) as

$$U_{(i)}=\left[\eta_1^{(i)}\quad\eta_2^{(i)}\quad\eta_3^{(i)}\quad\eta_{x1}^{(i)}\quad\eta_{x2}^{(i)}\quad\eta_{x3}^{(i)}\quad\Phi_1^{(i)}\quad\Phi_2^{(i)}\quad\Phi_3^{(i)}\quad\Phi_4^{(i)}\quad\Phi_5^{(i)}\right],\tag{22}$$

the global finite element matrix equation is

$$\begin{bmatrix}\mathbf{K}+\Omega\mathbf{C}-\Omega^2\mathbf{M} & \mathbf{B}^*\sqrt{\Omega^2-F^2}\\ \mathbf{B}\sqrt{\Omega^2-F^2} & i\sqrt{B(0)}\sqrt{\Omega^2-F^2}\end{bmatrix}\begin{bmatrix}\mathbf{U}\\ R\end{bmatrix}=\begin{bmatrix}-\mathbf{B}^T\sqrt{\Omega^2-F^2}\\ -i\sqrt{B(0)}\sqrt{\Omega^2-F^2}\end{bmatrix},\tag{23}$$

where, for a total of N finite elements it is $\mathbf{U}=\left[U_{(1)}\quad U_{(2)}\quad\ldots\quad U_{(N-1)}\quad U_{(N)}\right]^T$, $\mathbf{B}=\left[0\quad 0\quad 0\quad 0\quad\ldots\quad 0\quad 0\quad -i\sqrt{B(0)}\right]$, with $\mathbf{B}^*$ denoting the conjugate transpose and $\mathbf{B}^T$ the transpose. Matrices $\mathbf{K},\mathbf{C},\mathbf{M}$ are produced by the discretisation of the terms:

$\int_{-1}^{0}K(x)\bar{v}_{xx}\eta_{xx}dx+\int_{-1}^{0}\bar{v}\eta dx+\int_{-1}^{0}\left[B(x)-M(x)\right]\bar{w}_x\Phi_x dx$, $i\int_{-1}^{0}(\bar{v}\left[1-\left(F/\Omega\right)^2\right]\Phi-\bar{w}\eta)dx$ and $\int_{-1}^{0}M(x)\bar{v}\eta dx$, respectively.

4. ICE SHELF RESONANCES USING EIGENANALYSIS

To analyse the resonant vibrations of an ice-shelf/sub-ice-shelf cavity system as an eigenvalue problem, homogeneous conditions at the water interface between the open ocean and the ice shelf cavity are applied, i.e. $\Phi(0)=0$ or $\Phi_x(0)=0$. Using the latter Dirichlet or Neumann conditions in Eqs. (11) and (6) it is

$$\Psi(0)=R+1=0\Rightarrow R=-1\text{, or} \tag{24}$$

$$\Psi_x\big|_{x=0}=i\sqrt{\frac{\Omega^2-F^2}{B(0)}}(1-R)\Rightarrow R=1. \tag{25}$$

Condition (25) is the one employed by Sergienko (2013) and Meylan et al. (2017) for the study of normal modes of ice shelves. Sergienko (2013) justifies this selection based on the argument that no mass exchange must occur between the water in the cavity and the open ocean during the resonant vibrations of the ice shelf. Note that in both cases $R=-1$ and $R=1$ it is,

$$\begin{aligned}\left\|\sqrt{K}\eta_{xx}\right\|_{L^2}^2+\left\|\eta\right\|_{L^2}^2-\Omega^2\left\|\sqrt{M}\eta\right\|_{L^2}^2-\left(1-\left(F/\Omega\right)^2\right)\left\|\sqrt{B-M}u\right\|_{L^2}^2=\\=-2\Omega\left(1-\left(F/\Omega\right)^2\right)^{3/2}\sqrt{B(0)}\,\mathrm{Im}(R)=0.\end{aligned} \tag{26}$$

The objective of this section is to formulate both eigenvalue problems, in order to compare the eigenperiods with the characteristic periods obtained by the response of the ice shelf when the more realistic interface conditions are applied. The solution of the eigenvalue problems corresponding to conditions (24) or (25), can be performed analytically, or obtained numerically by means of the finite element method. The advantage of finite elements is that it can handle problems with variable seabed topography or ice-shelf thickness as well.

REMARK: In the examined shallow-water hydroelastic case, contrary to the case of a shallow basin without ice cover, the condition $\Phi(0)=0$ does not imply that the elevation/ice-shelf-deflection is zero at this point. It is noted that when $R=-1$, we have

$$u(0)=\frac{B(0)}{B(0)-M(0)}\Psi_x\big|_{x=0}=2i\frac{\sqrt{B(0)}}{B(0)-M(0)}\sqrt{\Omega^2-F^2}\,. \tag{27}$$

This velocity corresponds to the maximum amplitude out-charge (towards the water region) or in-charge (towards the hydroelastic region) flow values attained.

5. NUMERICAL RESULTS AND APPLICATIONS

Several cases will be presented and discussed in this section. First, two illustrative examples will be considered, for an ice shelf of relatively large length $150\ km$ and shorter one with length $50\ km$. In both cases, the depth of the oceanic basin at the free end of the ice-shelf is $b = 500\ m$, while the ice shelf thickness is $h = 300\ m$. The ice/water density ratio is $\rho_i / \rho_w = 0.9$ and the Young's modulus of ice is taken as $E = 11 GPa$. This value is used by Meylan et al. (2017) and is close to the range 8-10 GPa, which Schulson and Duval (2009) predicted by lab experiments. It should be noted that smaller values of Young's modulus ($\sim 1 GPa$) have been also used by several authors, e.g. Vaughan (1995). A more detailed discussion regarding Young's modulus values for ice shelves can be found in Lescarmontier et al. (2012) and Lee et al. (2018). In all cases, it is expected that Young's modulus values will not affect the hydroelastic response of large ice-shelves significantly, at least when the fundamental and lower modes are considered (Godin and Zabotin, 2016).

The response of the ice shelf will be evaluated using the potential energy norm

$$\|\eta\|_E = \left(\|\eta\|_{L^2}^2 + \left\| \sqrt{K} \eta_{xx} \right\|_{L^2}^2 \right)^{1/2}, \tag{28}$$

and the Chebyshev (maximum) type norm

$$\|\eta\|_{C^0} + \|K \eta_{xx}\|_{C^0}, \tag{29}$$

where $\|q\|_{C^0} = \max_{x \in [-1,0]} |q|$. The norm in Eq. (28) represents the potential energy of the ice shelf. In particular, the second term is the strain energy. The norm in Eq. (29) combines the maximum value of the deflection and the maximum value of the bending moment (in the non-dimensional setting).

These two norms will be calculated using the solution of the Reflection-Transmission problem and will be plotted against the period of the impacting waves. Along with these two norms, the eigenperiods of the ice-shelf/cavity system T_D, as predicted using the Dirichlet condition $\Phi(x=0)=0$, and T_N as predicted using the homogeneous Neumann condition $\Phi_x\big|_{x=0} = 0$, will be plotted. The objective is to examine whether T_D or T_N better predict the local maxima of the ice shelf response, especially as the principal (low-order) modes are concerned. Since we are interested in long wave forcing, only the first 20 characteristic periods will be examined at this stage. In all cases, 500 hydroelastic elements were used and convergence for the first 100 modes for meshes with more than 300 has been verified using extensive numerical experiments.

Next, the effects of main geometrical parameters on the first two characteristic periods will be examined and the predictive capability of simplified Dirichlet boundary conditions at the ice-water interface will be demonstrated. Finally, the present model will be applied to the cases of simplified models of the Ross and Larsen C Ice Shelves, examining also the effect of Coriolis frequency on the resonant frequencies for these Antarctic regions.

5.1 Illustrative Examples

a. Ice shelf with length $L = 150\ km$.

A relatively large ice shelf of length $L = 150\ km$ is examined first. The ice shelf response, along with the T_D and T_N eigenperiods are plotted in Fig. 3 as a function of the wave forcing period. The thick blue line corresponds to the ice shelf potential energy norm and the thick red line corresponds to norm defined by Eq. (29). The eigenperiods T_D are depicted using thick, continuous vertical lines and the eigenperiods T_N using thin, dashed vertical lines.

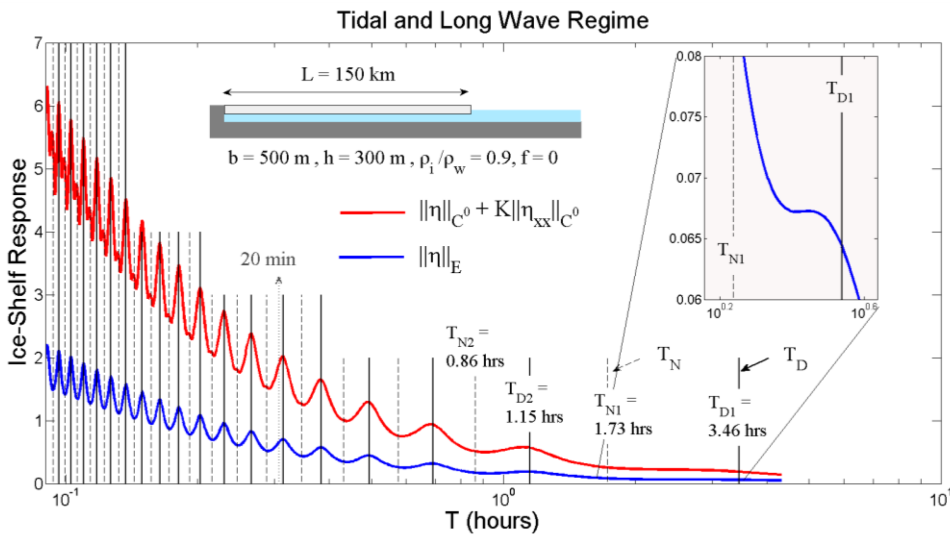

Figure 3. Response of an ice shelf with length $150\ km$ measured in the potential energy norm $\|\eta\|_E$ (blue line) and a maximum type norm (red line), as a function of the period of the incoming waves. Horizontal axis is in logarithmic scale. The first 20 eigenperiods corresponding to homogeneous Dirichlet (thick, black vertical lines) and homogeneous Neumann (dashed, black vertical lines) conditions are also plotted.

This is expected since the energy flow to the ice-shelf/cavity system has been found to be proportional to $\Omega\,\mathrm{Im}(R)$. The latter is proportional to the frequency of the impacting wave and also contains the oscillatory term $-1 \le \mathrm{Im}(R) < 1$, which creates several local maxima and minima in the response indicators. For higher frequency the energy norm exhibits a more regular behaviour than Chebyshev (maximum) type norm. Examining the relation between the eigenperiods of the system and the response, quantified by the potential energy norm, it is evident that T_D values correspond to local maxima locations of the response, while T_N values correspond to locations of local minima. This interesting observation holds for the first eigenperiods and is verified by the response in the maximum type norm as well. The approximation of the first local maximum by T_D (zoom box in Fig. 3) is not as accurate as that corresponding to the following peaks of the response. Still, the T_D value provides a considerably better approximation than T_N. In the case of the maximum type norm (red line), the response pattern becomes more irregular for periods less than approximately 20 min (indicated by a vertical arrow in Fig.3). For higher modes, T_N values coincide with localised maxima of small amplitude, but again the highest local peaks are determined by eigenperiods calculated using the Dirichlet condition $\Phi = 0$.

In Fig. 4 the real and imaginary part of the reflection coefficient, as computed using the finite element method is depicted. The results shown verify that eigenperiods T_D (vertical solid black lines) are characterised by $\mathrm{Re}(R) = -1$ and eigenperiods T_N (vertical dashed black lines) correspond to $\mathrm{Re}(R) = 1$.

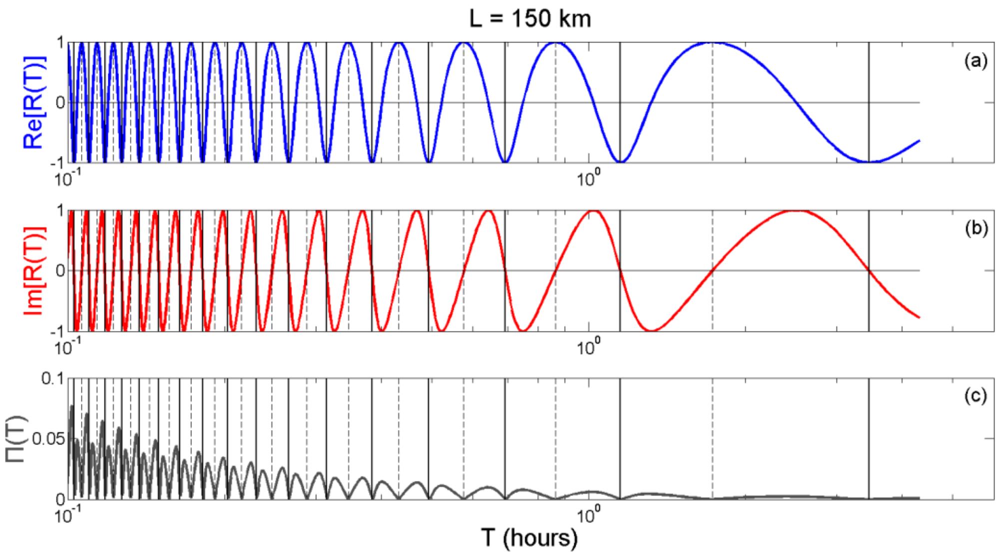

Figure 4. Ice-shelf with length 150 km. Real and imaginary part of the reflection coefficient R. (c) The energy difference Π as a function of the incoming wave period. Horizontal axis is in logarithmic scale.

In both cases, T_D and T_N it is $\mathrm{Im}(R) = 0$. The $\Pi(T)$-term defined in Eq. (19) is plotted in Fig. 4(c) as a function of the period of the incoming waves. The eigenperiods T_D and T_N are plotted again as vertical lines. The horizontal axis is in logarithmic scale. The local minima, corresponding to zero values of this quantity predict all the eigenperiods whether homogeneous Dirichlet or Neumann conditions are employed. This is compatible with the fact that at these periods it is $\mathrm{Im}(R)=0$ and no energy enters or leaves the ice-shelf region, according to the energy balance in Eq. (18).

Finally, the response of the ice-shelf, as predicted by the reflection-transmission model for forcing periods, corresponding to the first three predictions of Dirichlet and Neumann models, is shown in Fig. 5. The left column presents the real part and the right column the imaginary part of the normalised upper surface elevation $\eta_* = \eta / \max_{\mathrm{T}} \|\eta(\mathrm{T})\|_{C^0}$, where the maximum in the denominator is taken over the range of periods examined. As expected, the response becomes more oscillatory as the period of the incoming waves drops. The interesting observation is that when the forcing corresponds to a T_D eigenperiod, the amplitude of the real part is several orders of magnitude larger than the amplitude of the imaginary part. Conversely, when the forcing corresponds to T_N eigenperiods, the situation is reversed and it is the amplitude of the imaginary part that is several orders of magnitude larger.

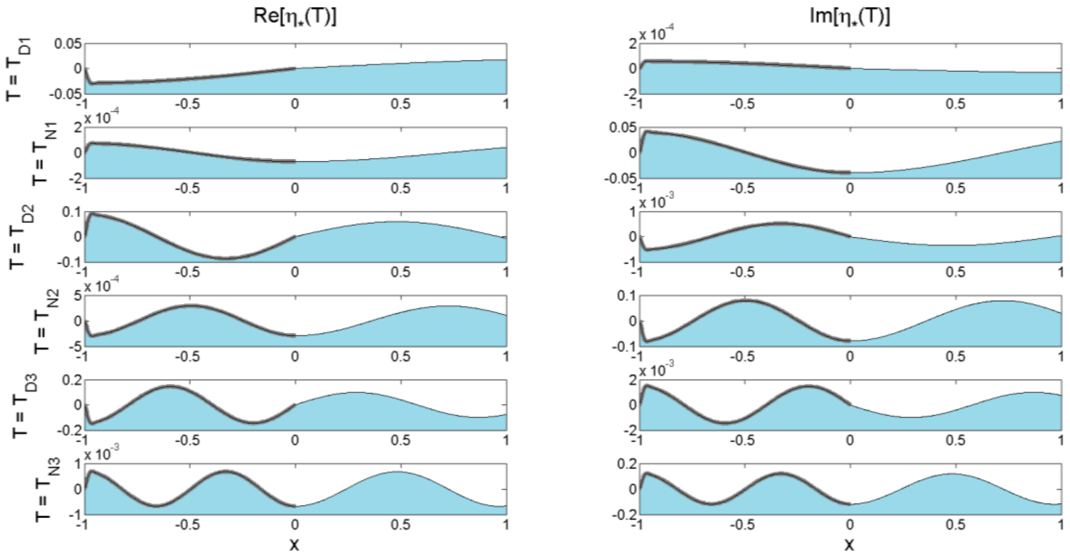

Figure 5. Ice-shelf with length 150 km. Real (left column) and imaginary (right column) part of the ice-shelf deflection as predicted by the reflection-transmission model. The wave forcing period corresponds to the first three Dirichlet and Neumann eigenperiods. Note the alternating difference in amplitude scales between the real and imaginary parts of the response.

b. Ice shelf with length $L = 50\ km$

In this example, a smaller ice shelf, with length $L = 50\ km$, is studied. Figure 6 depicts the response of this ice shelf using the same quantities and definitions as before. The spectrum of the shorter ice shelf is of course shifted to lower periods.

Again, in the case of the shorter ice-shelf, the T_D values correlate better that T_N with the local maxima of the ice-shelf response. However, this good correlation is only observed for the first 10 eigenperiods (when the potential energy norm is considered). The deviation between the T_D values and the peaks of the maximum type norm occurs after the sixth eigenperiod. For larger eigenperiods, the T_N eigenvalues appear to correspond to local minima locations of the potential energy norm. It can thus be stated that the use of the Dirichlet condition $\Phi = 0$ at the free end is preferable.

It is furthermore interesting to note that for small period values the T_D values approximate again better the norm peaks. However, in these shorter wavelengths, the gaps defined by the succession of T_D and T_N values become narrower, and both eigenvalue models are ultimately expected to provide good approximation provided that the long wave assumption still holds.

Again, the approximation of the first local maximum by T_D (zoom box in Fig. 6) is not as accurate as that corresponding to the following peaks of the response. Still, it provides a much better prediction of the first peak in the potential norm response than the first T_N eigenperiod.

Figure 7 depicts the real and imaginary part of the reflection coefficient, as computed using the finite element method. The $\Pi(T)$-term defined in Eq. (19) is plotted in Fig. 4(c) as a function of the period of the incoming waves. Again, the minimisation of this quantity holds for both T_D and T_N eigenperiods, where the value attained is zero, according the prediction of Eq. (18). Finally, the theoretical prediction that T_D values correspond to $\mathrm{Re}(R) = -1$ and T_N values correspond to $\mathrm{Re}(R) = 1$, while in both cases it is $\mathrm{Im}(R) = 0$, is verified by the numerical results for the reflection coefficient shown in Fig. 7.

The deflection of the ice-shelf, as predicted by the reflection-transmission model for forcing periods corresponding to the first three predictions of Dirichlet and Neumann models is shown in Fig. 8. Again the real part (left column) and the imaginary part (right column) of the normalised upper surface elevation $\eta_* = \eta / \max_{\mathrm{T}} \|\eta(\mathrm{T})\|_{C^0}$, is plotted.

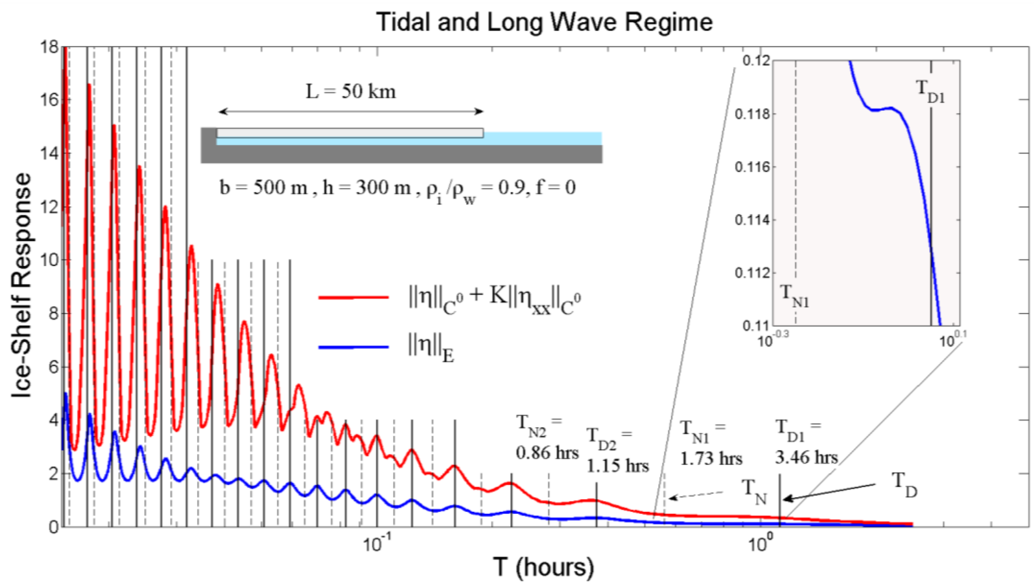

Figure 6. Response of an ice shelf with length $50\ km$ measured in the potential energy norm $\|\eta\|_E$ (blue line) and a maximum type norm (red line), as a function of the period of the incoming waves. The first twenty eigenperiods corresponding to homogeneous Dirichlet (thick, black vertical lines) and homogeneous Neumann (dashed, black vertical lines) conditions for the velocity potential are also plotted.

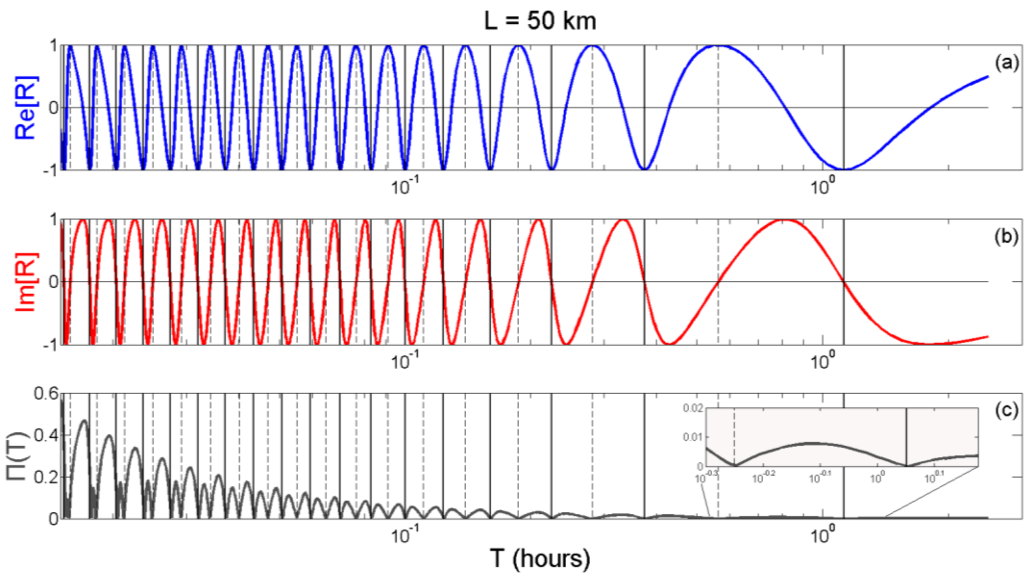

Figure 7. Ice-shelf with length $50\ km$. (a) The quotient Q of an as a function of incoming waves period. (b). Real and imaginary part of the reflection coefficient R Horizontal axis is in logarithmic scale.

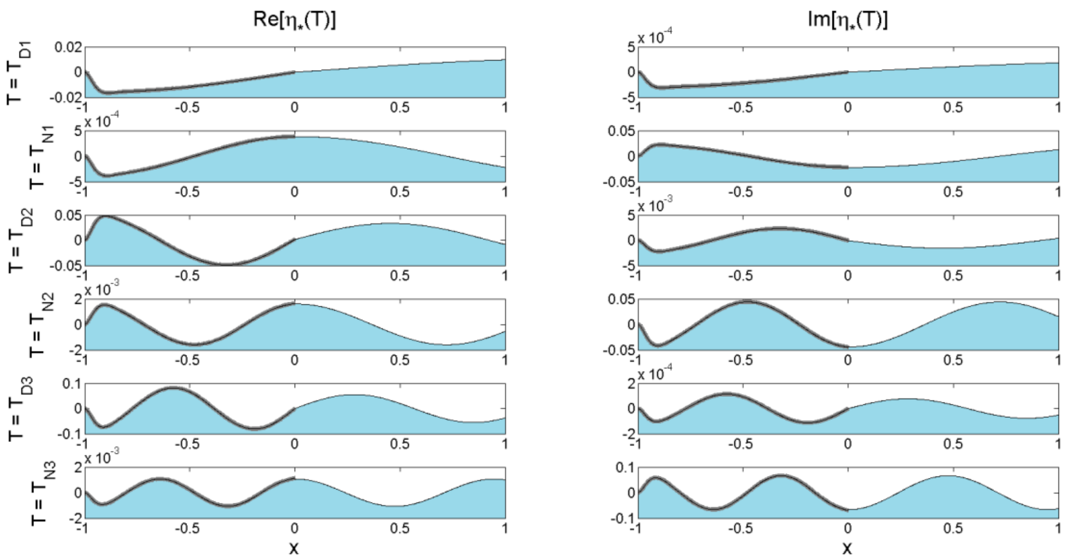

Figure 8. Ice-shelf with length $50\ km$. Real (left column) and imaginary (right column) part of the ice-shelf deflection as predicted by the reflection-transmission model. The wave forcing period corresponds to the first three Dirichlet and Neumann eigenperiods. Note the alternating difference in amplitude scales between the real and imaginary parts of the response.

Similarly to the case $L = 150\ km$, when the forcing corresponds to a T_D eigenperiod, the amplitude of the real part is several orders of magnitude larger than the amplitude of the imaginary part. Conversely, when the forcing corresponds to T_N eigenperiods, the situation is reversed and it is the amplitude of the imaginary part that is several orders of magnitude larger.

5.2 Systematic investigation of the main geometrical parameters

In Fig.9 results from systematic investigation are presented in order to illustrate the effects of main geometrical parameters, as the ice shelf length, its thickness and the water depth, on the predicted eigensolution, in the case of an ice shelf – water system. In particular, contour plots of the first and second characteristic periods are shown (in non-dimensional form $10^{-3}T_{1,2}\sqrt{L/g}$) with respect to ice-shelf length over water depth L/b ranging from 50 to 500, and thickness ratio h/b taking values from 0.1 to 0.6, respectively. For calculations, the ice/water density ratio considered is $\rho_i/\rho_w = 0.9$ and the Young's modulus of ice is $E = 11\text{GPa}$ while the water depth is set to 500m. Results obtained by the maximization of the considered norms are shown by solid lines, while predictions based on the application of Dirichlet boundary condition are plotted by using dashed lines.

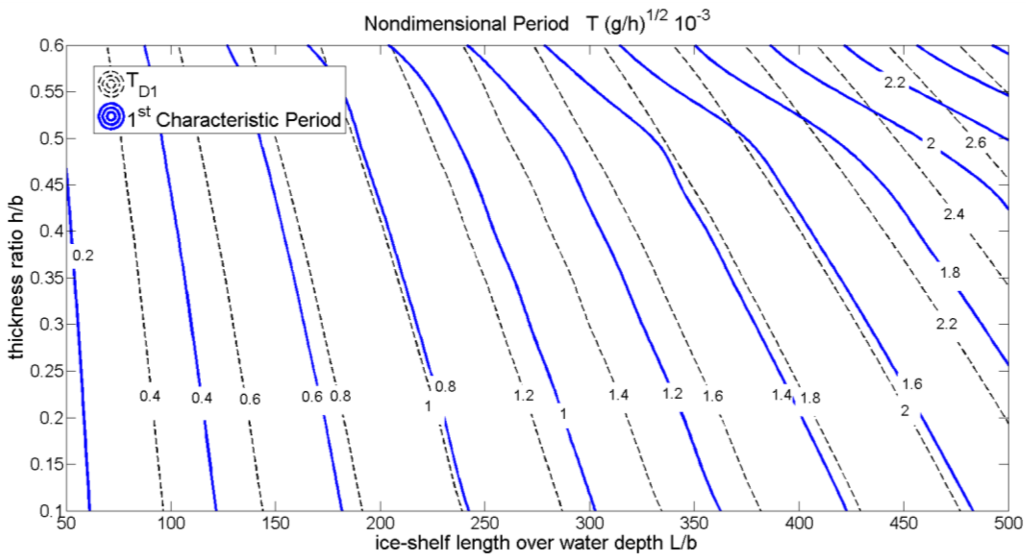

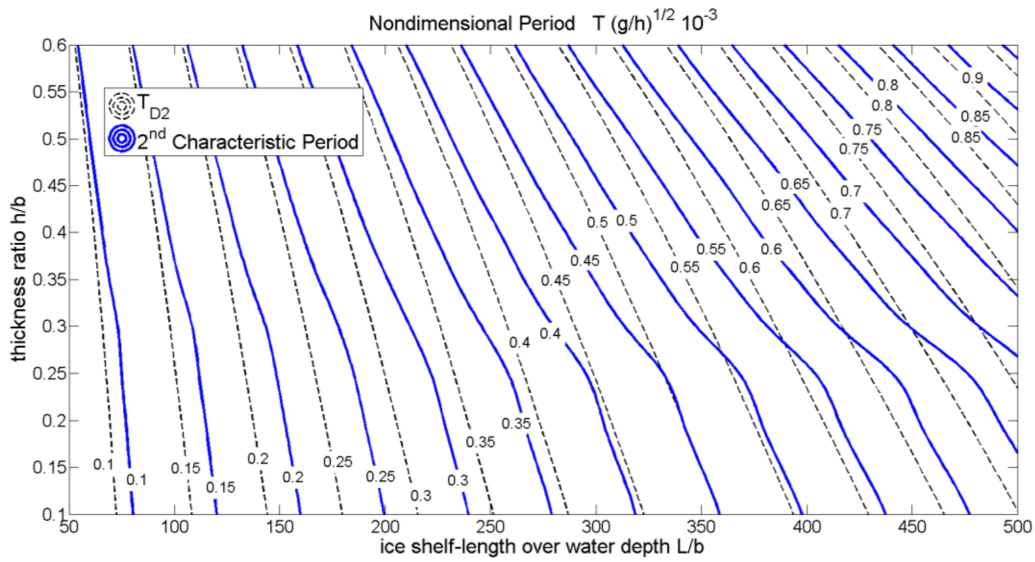

Figure 9. Effect of geometrical parameters on the 1st and 2nd characteristic periods. Solid line present solution based on the max norm, Dashed lines indicate predictions by means of eigenvalue analysis using Dirichlet boundary conditions.

In general, Dirichlet boundary conditions are capable of providing quite reasonable predictions of the most important first two characteristic periods. Differences reaching 10-15% with the values obtained by the maximization of responses by the considered norms are observed, especially as the ice shelf thickness and length substantially increase. Also, we note that as the mode index increases the observed differences become smaller. Finally, a trend is observed concerning the characteristic periods corresponding to maximum responses, since they appear to switch between Dirichlet eigenperiods as the thickness ratio varies. This feature could be due to fuzziness of maximum responses concerning the first modes (see also Fig.3), and is left to be more thoroughly investigated in future work.

5.3 A model for the Ross Ice Shelf

The response of an ice shelf with length $L = 550\ km$ and thickness $h = 300\ m$ will be studied. These values have also been used by Godin and Zabotin (2016) to analyse the eigenperiods of the Ross Ice Shelf. The bathymetric profile described by Fretwell et al. (2013) and also depicted in Brominski et al. (2015) for a cross section of the ice-shelf-water cavity geometry along a transect approximately orthogonal to the Ross Ice Shelf front will be used. In particular, the depth profile will be set to

$$b(x) = 700 - 10000\left(\frac{x}{L}\right)^2\left(1+\frac{x}{L}\right)^6 \quad m, \tag{30}$$

which yields a reasonable approximation of the variable seabed topography. A satellite image of the Ross Ice Shelf is shown in Fig. 10(a), with the considered cross-section denoted by a thick green line. Figure 10(b) shows the basic geometry and seabed topography characteristics of the model. A more sophisticated model of the Ross Ice Shelf has been recently presented by Sergienko (2017).

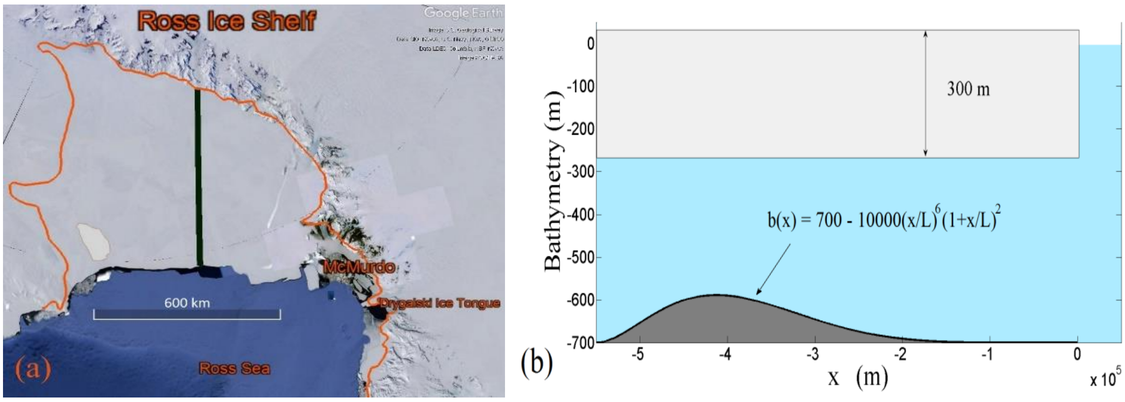

Figure 10. (a) The Ross Ice Shelf. (b) Approximation of the ice shelf and cavity seabed topography along a transect (see also Brominski et al. 2015).

The ice shelf response in the potential energy and maximum type norm is shown in Fig. 11. The first 20 eigenperiods T_D and T_N are also plotted. Again the local maxima of the response coincide with the eigenperiods T_D. The largest eigenperiod $T_{D1} = 9.60\ hours$ is approximately twice the corresponding one $T_{N1} = 4.99\ hours$. The value $T_{D1} = 9.60\ hours$ is very close to the value $9.8\,hours$ obtained by Godin and Zabotin (2016). In the latter work it is pointed out that this resonance value is very close to the largest period of the persistent atmospheric waves observed in the Ross Ice Shelf region ($\sim 10\,hours$) and the very interesting theory that the two phenomena could be interrelated is proposed.

In their analysis Godin and Zabotin (2016) used a constant bathymetry profile. In order to derive a homogenised environment for the present hydroelastic analysis, the mean depth

$$\int_{-1}^{0}\left(700-10000x^{6}(1+x)^{2}\right)dx = 660.32\ m\,, \tag{31}$$

will be considered. Keeping all other parameters the same and solving for the constant depth $b_m = 660\ m$ the response depicted in Fig. 12 occurs. In this case, the first observed characteristic periods, indicated by the maxima of the norms (Eqs. 28 and 29) are approximately: 8.00, 3.05, 1.92 hours. It is observed that the relative difference between the eigenperiods predicted by the variable bathymetry and constant bathymetry (based on the mean depth) is small. Regarding the first 50 modes, the relative difference between the two models is always less than 2.5% with the largest deviations appearing in the first two modes. Based on the above results, the approximate use of an averaged depth in cases characterised by mild seabed variations is expected to provide reasonably good approximations.

Next, in Fig.13, the Coriolis effect on the calculated characteristic periods is presented for the above constant depth idealized model of the Ross Ice Shelf. We consider a mean value of Coriolis frequency, which at latitude 80deg South is estimated to be $1.432\ 10^{-4}\ rad/\sec$ (corresponding to 12.2 hours). The changes are substantial and the first three resonant characteristic periods (corresponding to the peaks of the norms) in Fig.12 are approximately: 6.60, 3.00 and 1.90 hours, respectively. Moreover, it is observed that the homogeneous Dirichlet boundary conditions are able to provide reasonable predictions.

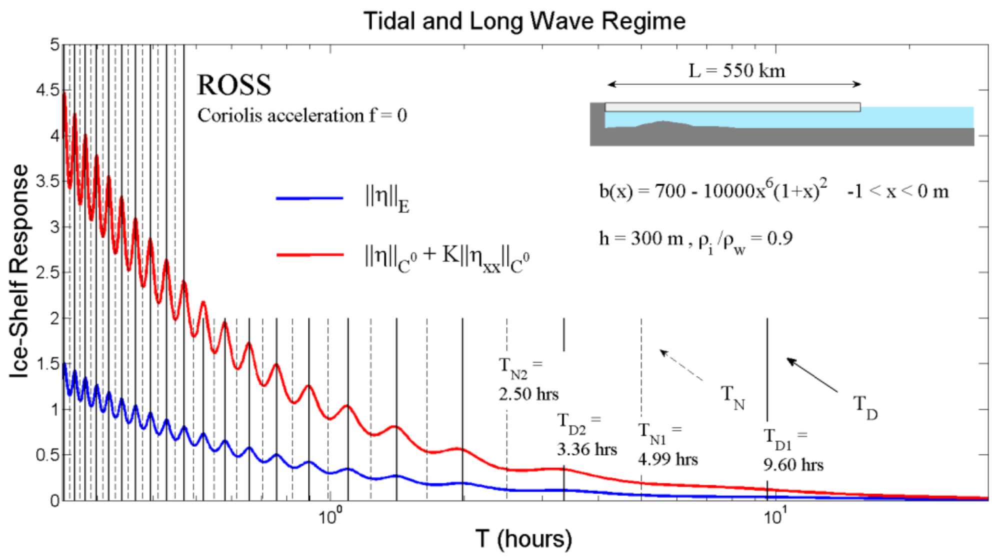

Figure 11. Response of the Ross Ice Shelf model, measured in the potential energy norm $\|\eta\|_E$ (blue line) and a maximum type norm (red line), as a function of the period of the incoming waves. The first twenty eigenperiods corresponding to homogeneous Dirichlet (thick, black vertical lines) and homogeneous Neumann (dashed, black vertical lines) conditions for the velocity potential are also plotted.

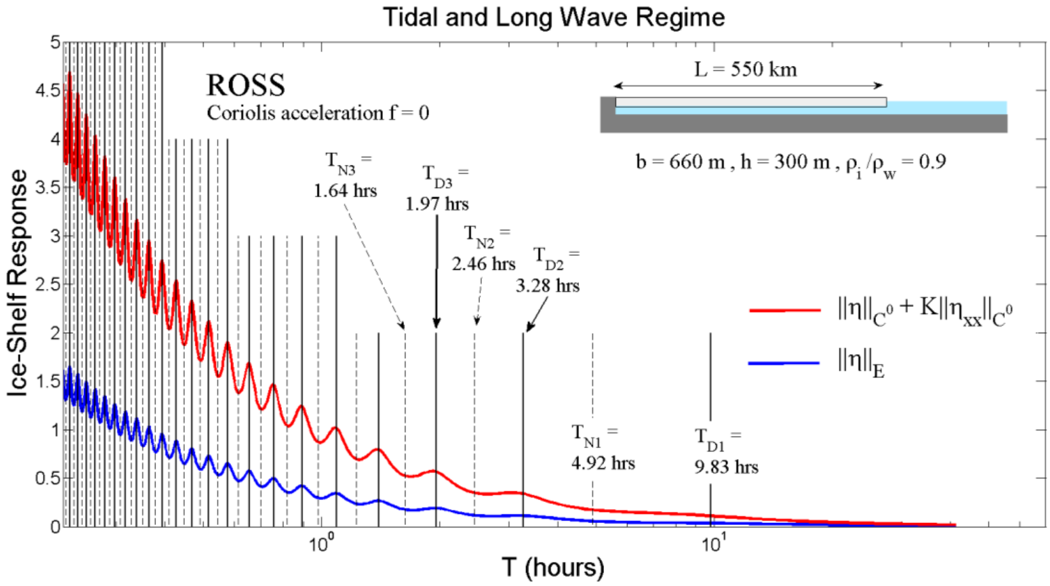

Figure 12. As in Fig. 11, but with constant cavity depth $b = b_m = 660\,m$.

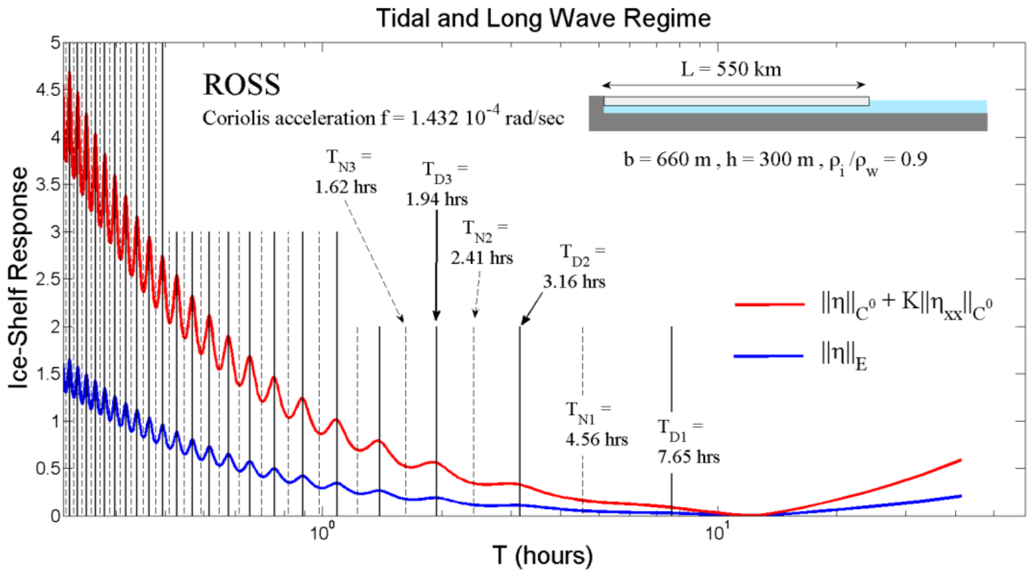

Figure 13. As in Fig.11, but with the Coriolis effects for an average latitude of 80deg South.

Concluding this section, it is interesting to note that when the Coriolis acceleration is included, the present model is able to provide reasonable predictions above the cut-off frequency. Also, for large domains, the present FEM model supports the study of additional effects due to spatial variability of the Coriolis frequency and this is left to be presented in future work.

5.4 A model for the Larsen C Ice Shelf

The response of an ice shelf with length $L = 200\ km$ and thickness $h = 300\ m$ will studied in this section. The uniform depth is set to $b = 500\,m$. This particular set of values are chosen to represent, in the mean, the characteristics of the Larsen C Ice Shelf along the transect depicted in Fig 14(a), by the green line (Griggs and Bamber, 2009). The ice shelf density for this case is $\rho_i = 917\ kg/m^3$ and the water density $\rho_w = 1027\ kg/m^3$. As before the value for Young's modulus is set to $E = 11GPa$.

Figure 14(a) is a satellite image of the Larsen C Ice Shelf, where the cross-section considered is shown approximately with a solid green line. The geometric characteristics of the adopted model, namely average thickness and seabed topography are shown in Fig. 14(b). The response of the present model used for the simulation of Larsen C hydroelastic resonant behaviour without Coriolis effects is illustrated in Fig. 15. The potential energy norm and maximum type norm curves are quite similar to those corresponding to the ice shelf with length $150\,km$ as the bathymetric and thickness profile are the same in both cases and the span is comparable. The first 3 characteristic periods identified by the maxima of the norms, defined by Eqs.(28) and (29), are approximately 3.90, 1.51, 0.91 hours, respectively. The first T_D eigenperiods, using the zero velocity potential condition at the cavity below the ice shelf front are again found in very good match with the local maxima of the potential and maximum type norms of the cantilever response.

The fundamental eigenperiod is now $T_{D1} = 4.61\ hours$, while the second eigenperiod is calculated at $T_{D2} = 1.54\ hours$. These values are slightly less than half of the respective values of the Ross Ice Shelf model.

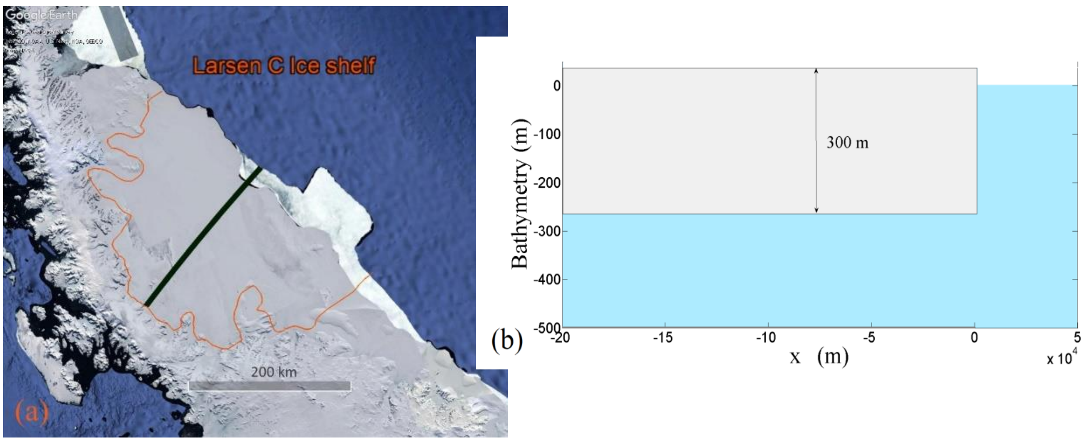

Figure 14. (a) The Larsen C Ice Shelf. (b) Approximation of the ice shelf and cavity seabed topography along a transect (see also Griggs and Bamber, 2009).

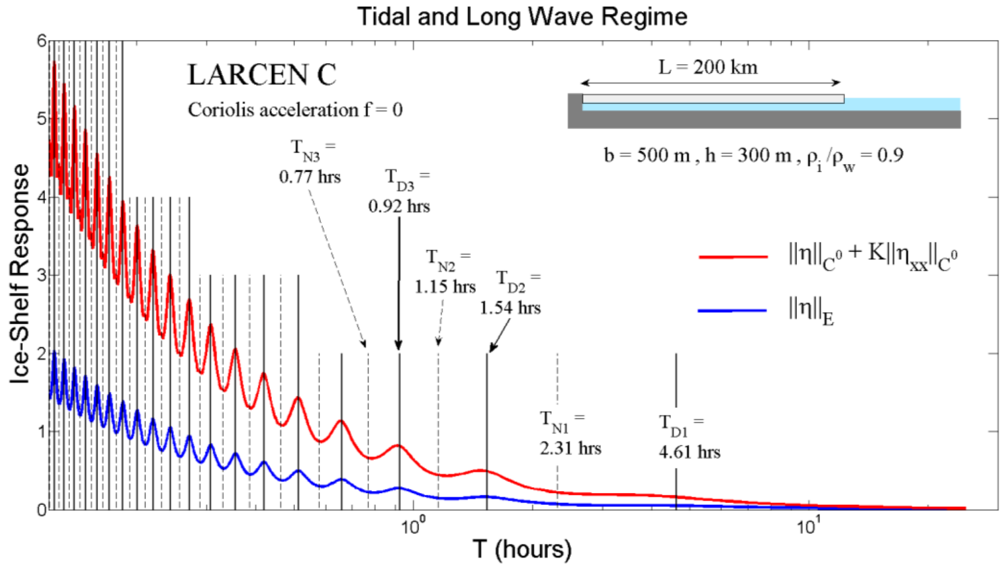

Figure 15. Response of the Larsen C Ice Shelf model, measured in the potential energy norm $\|\eta\|_E$ (blue line) and a maximum type norm (red line), as a function of the period of the incoming waves. The first twenty eigenperiods corresponding to homogeneous Dirichlet (thick, black vertical lines) and homogeneous Neumann (dashed, black vertical lines) conditions for the velocity potential are also plotted.

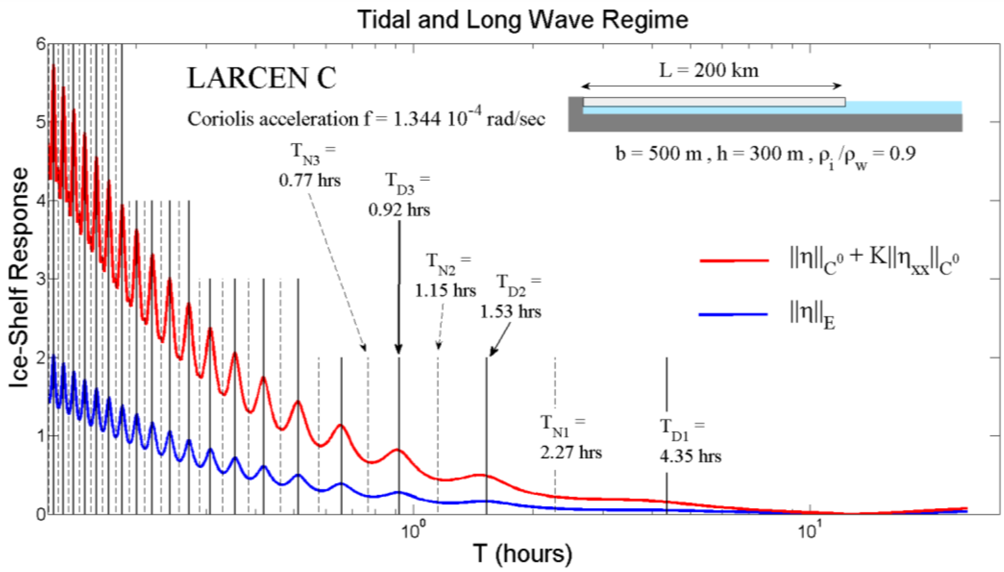

Figure 16. As in Fig.15, but with the Coriolis effects for an average latitude of 67.5deg South.

Finally, for the above model of the Larsen C Ice Shelf, the Coriolis effect on the characteristic periods is presented in Fig.16. We consider a mean value of Coriolis frequency which at a mean latitude 67.5deg South is estimated to be

$1.344\,10^{-4}\ rad/\sec$ corresponding to approximately 13 hours in this case. The first three resonant periods which can be observed now by the present model are approximately: 3.60, 1.51, 0.91 hours, respectively. The changes are smaller than the ones observed in the case of the Ross ice shelve model, which is justified by the smaller value of latitude of the Larsen C ice shelve model. Similarly as before, the Dirichlet boundary conditions are able to provide quite reasonable predictions.

TO APPEAR IN OCEAN MODELLING 2018, https://doi.org/10.1016/j.ocemod.2018.10.008

6 APPROXIMATE PREDICTION OF EIGENPERIODS

Simple formulas for the approximation of the hydroelastic eigenperiods can be derived in homogeneous environments if the cavity basin without the ice shelf is considered, or if the ice shelf is modelled as a simple cantilever Euler-Bernoulli beam vibrating in vacuum; see Fig.17. In fact, using Eqs. (7) and (8) it is observed that for small Ω and small values of K, that are typical for ice shelves the above system reduces to shallow water equations. In the case of the cavity basin, an appropriate depth reduction can be applied to take into account the ice shelf draft as shown in Fig. 14. On the other hand, for larger values of Ω and thus highly oscillatory responses, $\left(K\eta_{xx}\right)_{xx}$ also becomes significant, and the above system reduces to the thin plate model. In both cases, the effects of the grounding line are assumed to be localised, in the sense that the hinge zone is considered very small compared to the length of the ice shelf, and can therefore be ignored. The same simplification has been applied to the hydroelastic model as well.

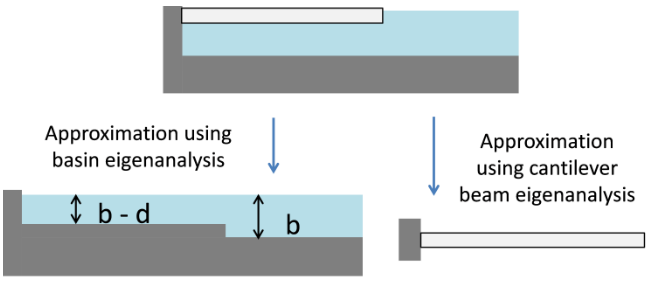

Figure 17. Two models for the approximation of the hydroelastic eigenperiods.

Considering the eigenanalysis of the cavity basin, a problem in the linearised shallow water theory occurs. The velocity at the grounding line and the velocity potential at the basin front are set to zero, resulting (in the nondimensional setting) in the formula

$$\Omega_{a,n} = \pi\left(n+1/2\right)\sqrt{B-M}\,, \qquad n = 0,1,2,\dots\,, \tag{32}$$

which by incorporating the Coriolis effect results in the form $\Omega_{c,n} = \sqrt{\Omega_{\alpha,n}^2 + F^2}$, in conformity with Godin & Zabotin (2016, Eq. 41). Hence, using the Dirichlet condition $\Phi = 0$ at the ice-shelf cavity/ocean interface, the eigenperiods can be approximated as follows:

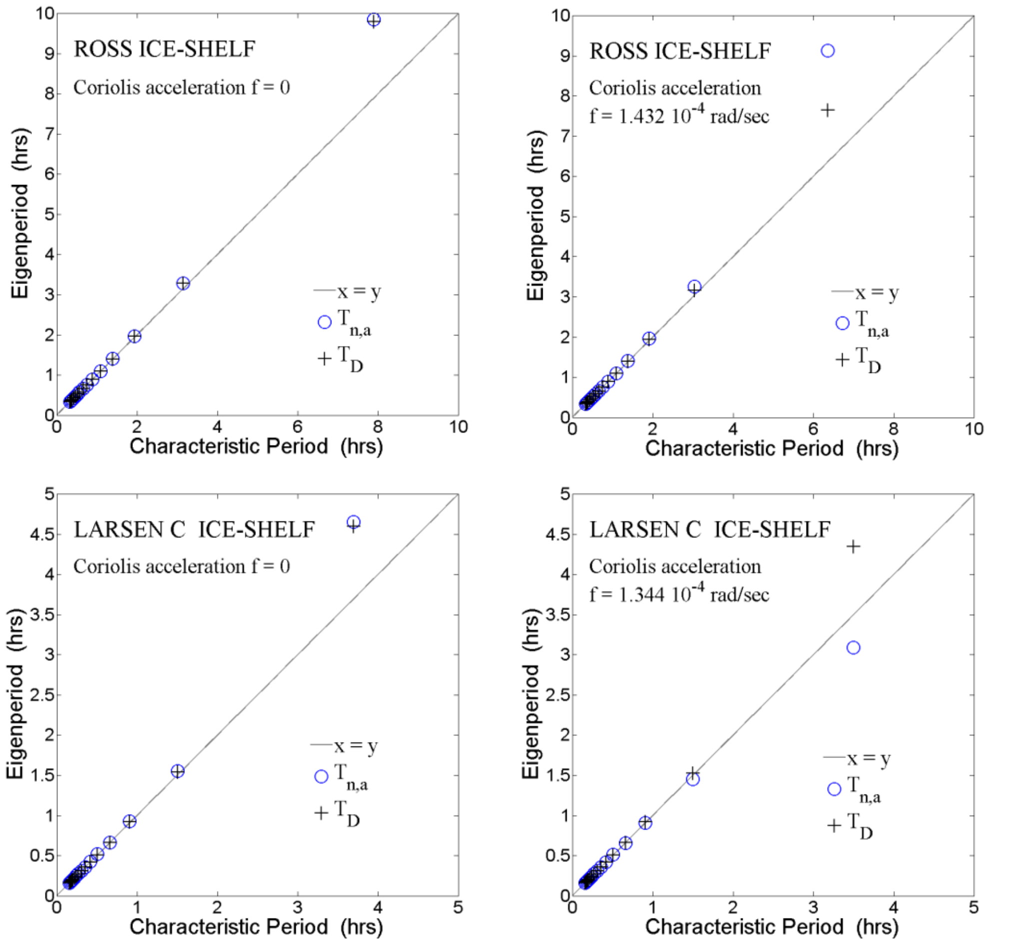

Figure 18. Prediction of resonant periods by means of approximate formula Eq. (33) and T_D values for the Ross ice-shelve model (first row) and Larsen C ice-shelve (second row). In the left column subplots the Coriolis effect is included.

- Approximation using cavity basin eigenanalysis

$$\mathrm{T}_{n,a} = \frac{1}{1800\sqrt{(n+1/2)^2\left(1-(\rho_i/\rho_w)(h/b)\right)+\left(f^2L^2/gb\right)}}\frac{L}{\sqrt{gb}}\ hours\,. \qquad (33)$$

It is noted here that the above equation contains the effect of reduced water depth under the ice shelf, as it accounts for its draft. The latter, however, being dependent on the ice mass distribution, includes the inertia characteristics of the ice shelf. It will be demonstrated in the sequel that the above formula produces reasonably accurate results that are close to those of the full hydroelastic model, particularly for ice shelves of large length.

The effectiveness of formula (33) is first assessed with respect to its capability to reproduce the characteristic periods occurring from the potential energy norm maximisation, compared to the predictions T_D. In particular, in Fig. 18, the characteristic periods of the Ross ice-shelf (first row) and the Larsen C ice-shelf (second row) are plotted against the eigenperiods obtained by Eq. (33) and those predicted using the Dirichlet condition on the wave potential $\Phi = 0$, namely T_D. The $T_{n,a}$ eigenperiods are denoted by circles and the T_D eigenperiods using crosses. The results of the right column include the Coriolis effect. In all cases, the 15 first characteristic periods and eigenperiods are shown. If the eigenanalysis models were capable of exactly reproducing the characteristic frequencies, all the results would lie on the principal diagonal. This is the case for periods larger than the second characteristic one. The predictions of formula (33) are excellent for the second characteristic period as well. The accuracy deteriorates when the fundamental eigenperiod is considered. However, the accuracy of Eq. (33) is still comparable to that of the hydroelastic eigenperiods T_D.

Using now the eigenperiods of a cantilever beam, the following result is obtained:

- Approximation using cantilever beam eigenanalysis

$$\mathrm{T}_{n,b} = \frac{\pi L^2}{1800\,\beta_n^2 h}\sqrt{\frac{12(1-v^2)\rho_i}{E}} \quad hours\,, \tag{34}$$

where β_n are the roots of the transcendental equation $1+\cos(\beta_n)\cosh(\beta_n)=0$.

A comparison of formulae (33) and (34) with the hydroelastic eigenperiods T_D, for the examples analysed in Section 5.1 and the Ross and Larsen C ice-shelves (without the Coriolis effect) is shown in Fig. 19. Both axes are in logarithmic scale. It is observed that the free basin approximation $T_{n,a}$ is very robust for the fundamental and lower modes. As the mode number increases, the quality of this approximation deteriorates. This is more evident in the case of smaller length ice shelves, while for very large ones, the free basin approximation is very good even for higher modes. A total of 100 modes are examined in Fig. 19. As the number of modes increases and the length of the ice shelf decreases, the hydroelastic eigenperiods are better approximated by those of the Euler-Bernoulli beam, namely $T_{n,b}$. Asymptotically, as $n \to \infty$, it is $T_{n,a} \sim 1/n$ and $T_{n,b} \sim 1/n^2$. Notably, for all examined ice shelf lengths, there was a set of modes for which neither model was proven accurate. This stresses the importance of employing hydroelastic eigenanalysis for the study of the resonant response of ice shelves. In all cases caution is needed to ensure that the assumptions of shallow water theory remain valid for the eigenstates corresponding to large mode numbers.

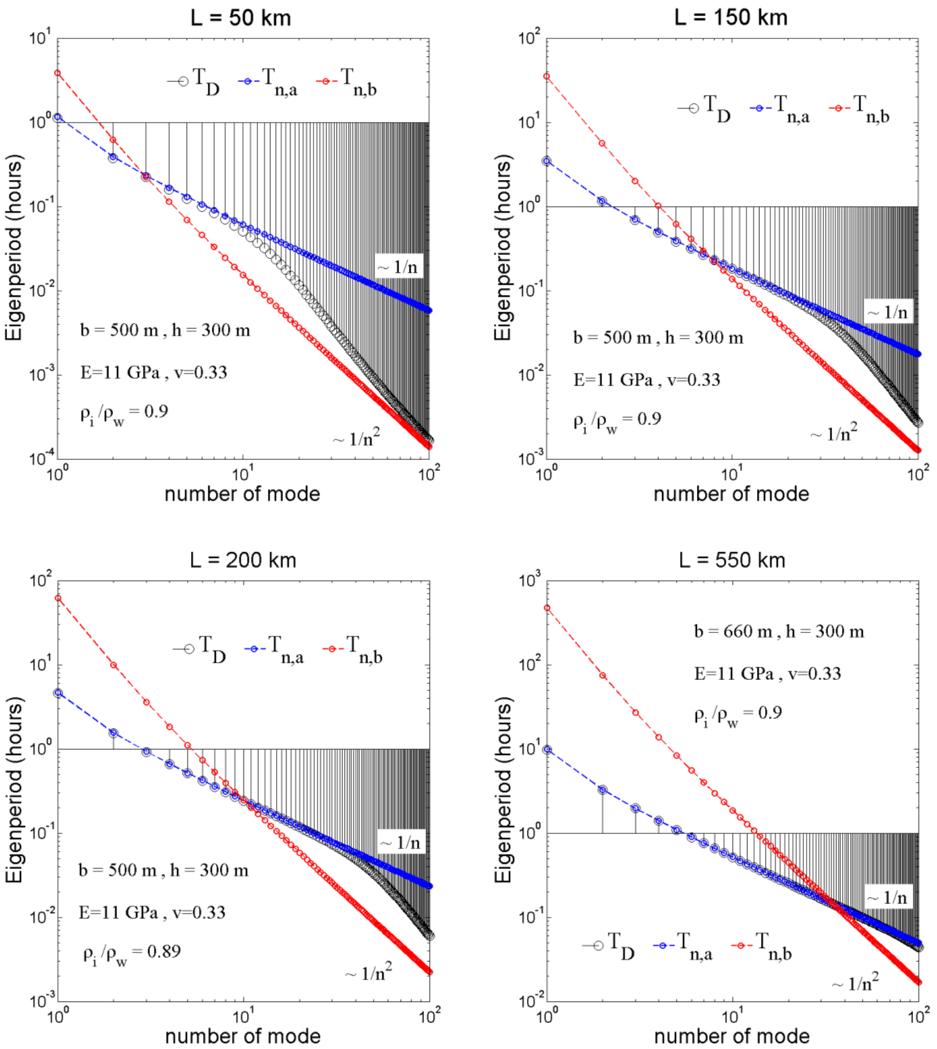

Figure 19. Approximation of the hydroelastic eigenperiods T_D using the eigenperiods of the cavity basin with no floating ice shelf $T_{n,a}$, with $f=0$ and using the eigenperiods of the ice shelf simulated by a cantilever beam in vacuum $T_{n,b}$ (for Coriolis acceleration $f=0$).

Since the free basin approximation of the eigenperiods yields quite accurate results for the fundamental and lower order modes, it is worthwhile investigating this approximation further. Figure 20 shows the relative difference of the basin eigenperiods $T_{n,a}$ and the hydroelastic eigenperiods $T_D = T_n$, as a function of the mode number, for different ice-shelf lengths and different thickness to depth ratios. The cases $L = 25, 50, 150, 300\ km$ are examined. The Coriolis effect is not included in this specific comparison. It is observed that the quality of the approximation deteriorates as the length of the ice-shelf decreases and the thickness to depth ratio h/b increases.

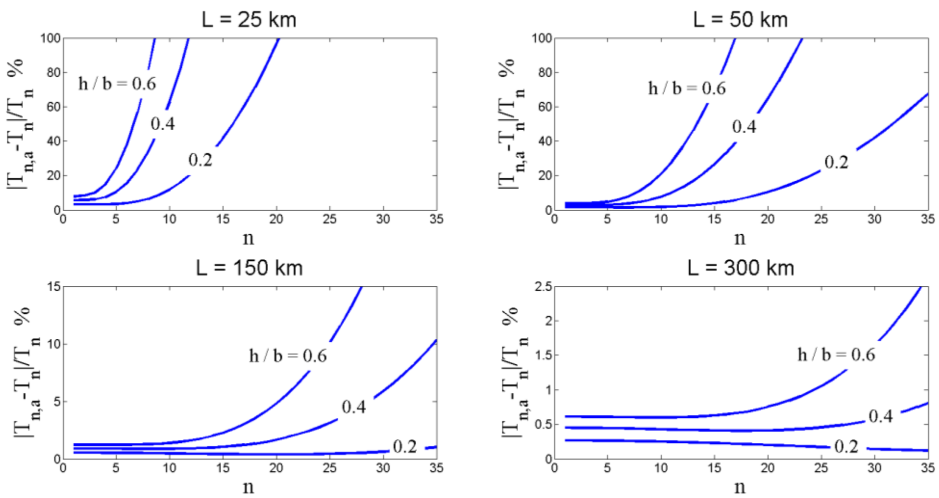

Figure 20. Relative difference of the basin eigenperiods $T_{n,a}$ and the hydroelastic eigenperiods $T_D = T_n$, as a function of the mode number, for different ice shelf lengths and different thickness to depth ratios (with Coriolis acceleration $f = 0$).

CONCLUSIONS

In the present work, the resonant hydroelastic vibrations of an ice-shelf/sub-ice-shelf cavity configuration are studied by employing shallow water theory, in conjunction with a thin plate model. The hydroelastic problem is formulated and solved as a wave Reflection-Transmission one, using higher-order FE that enable a fast and accurate computation of characteristic periods. The latter are considered as the forcing periods that maximise specific norms of the ice shelf response. The above numerical results are compared to solutions derived using specific homogeneous boundary conditions for eigenproblems of resonant ice shelf vibrations. We establish that appropriate homogeneous conditions on the wave potential, applied at the ice shelf front produce eigenfrequencies that, in general, agree well with the norm maximisation frequencies, also in the low frequency regime. Subsequently, the present methodology is applied to the prediction of characteristic periods of the Ross and Larsen C ice shelves providing eigenperiods in agreement with previously derived results by Godin and Zabotin (2016). The following key observations summarise the basic findings:

(i) The resonant behaviour of ice shelves, when the interaction with the surrounding ocean wave field is taken into account, is dominated by characteristic periods that maximise specific norms of the ice shelf oscillatory response.

(ii) A homogeneous Dirichlet condition for the wave potential at the ice shelf front was found to be the more accurate for hydroelastic eigenproblems. This result could be very significant when more elaborate 2D horizontal models for ice shelves of complex geophysical characteristics are considered. In this case, the Reflection-Transmission problem is very computationally demanding and the use of a homogeneous boundary condition at the ice shelf front significantly facilitates the numerical solution and analysis.

(iii) Approximate formulas for the hydroelastic eigenproblem of either a basin without the ice cover or only the ice shelf, modelled as an elastic cantilever, work well at different frequency bands. At small frequencies, the basin approximation is better, especially when large ice shelves are considered.

Of particular interest is the possibility to employ shallow-water models, already used for harbours and semi-enclosed basins, in the study of ice shelves by ignoring the ice cover as a first approximation. The present work suggests that this could be a reasonable approach for the estimation of the fundamental and lower-order modes, and will be exploited in future studies focusing on the eigenanalysis of realistic ice shelf configurations. Finally, the Coriolis acceleration could have important effects concerning the resonant modes of ice shelves in polar regions. In particular, the present model is shown to provide useful information for frequencies higher than the Coriolis frequency, and that the use of homogeneous Dirichlet boundary condition at the ice-shelf front is still able to provide good predictions.

REFERENCES

Ardhuin, F., Aksenov, Y., Benetazzo, A., Bertino, L., Brandt, P., Caubet, E., Chapron, B., Collard, F., Cravatte, S., Dias, F., Dibarboure, G., Gaultier, L., Johannessen, J., Korosov, A., Manucharyan, G., Menemenlis, D., Menendez, M., Monnier, G., Mouche, A., Nouguier F., Nurser G., Rampal, P., Reniers, A., Rodriguez, E., Stopa, J., Tison, C., Tissier, M., Ubelmann, C., van Sebille, E., Vialard, J., Xie, J.,2017. Measuring currents, ice drift, and waves from space: the Sea Surface KInematics Multiscale monitoring (SKIM) concept. Ocean Sci. 1-26. https://doi.org/10.5194/os-2017-65.

Bromirski, P. D., Chen, Z., Stephen, R. A., Gerstoft, P., Arcas, D., Diez, A., Aster, R. C., Wiens, D. A., Nyblade, A., 2017. Tsunami and infragravity waves impacting Antarctic ice shelves. J. Geophys. Res. 122 (7).https://doi.org/10.1002/2017JC012913

Bromirski, P. D., Sergienko O. V., MacAyeal D. R., 2010. Transoceanic infragravity waves impacting Antarctic ice shelves. Geophys. Res. Lett. 37 (2), L02502. https://doi.org/10.1029/2009GL041488.

Bromirski, P. D., Stephen, R. A., 2012. Response of the Ross ice shelf, Antarctica, to ocean gravity-wave forcing. Ann. Glaciol. 53 (60), 163–172. https://doi.org/10.3189/ 2012AoG60A058.

Bromirski, P.D, Diez, A., Gerstoft, P., Stephen, R. A., Bolmer, T., Wiens, D. A, Aster, R. C., Nyblade, A., 2015. Ross ice shelf vibrations. Geophys. Res. Lett. 42 (18), 7589–7597. https://doi.org/10.1002/2015GL065284

Brunt, K. M., Okal, E. A., MacAyeal, D. R., 2011. Antarctic ice-shelf calving triggered by the Honshu (Japan) earthquake and tsunami, March 2011. J. Glaciol. 57 (205), 785-788.

Chen, C., Chu, X., Zhao, J., Roberts, B. R., Yu, Z., Fong, W., Lu X., Smith, J. A., 2016. Lidar observations of persistent gravity waves with periods of 3–10 h in the Antarctic middle and upper atmosphere at McMurdo (77.83°S, 166.67°E). J. Geophysical Research Space Phys. 121 (2), 1483–1502. https://doi.org/10.1002/ 2015JA022127.

Fretwell, P., Pritchard. H. D., Vaughan, D. G., Bamber, J. L., Barrand N. E., Bell, R., Bianchi ,C., Bingham, R. G., Blankenship, D. D., Casassa, G., Catania, G., Callens, D., Conway, H., Cook, A. J., Corr, H. F. J., Damaske, D., Damm, V., Ferraccioli, F., Forsberg, R., Fujita, S., Gim, Y., Gogineni, P., Griggs, J. A., Hindmarsh, R. C. A., Holmlund, P., Holt, J. W., Jacobel, R. W., Jenkins, A., Jokat, W., Jordan, T., King, E. C., Kohler, J., Krabill, W., Riger-Kusk, M., Langley, K. A., Leitchenkov, G., Leuschen, C., Luyendyk, B. P., Matsuoka, K., Mouginot, J., Nitsche, F. O., Nogi, Y., Nost, O. A., Popov, S. V., Rignot, E., Rippin, D. M., Rivera, A., Roberts, J., Ross, N., Siegert, M. J., Smith, A. M., Steinhage, D., Studinger, M., Sun, B., Tinto, B. K., Welch, B. C., Wilson, D., Young, D. A., Xiangbin, C., Zirizzotti, A., 2013. Bedmap2: improved ice bed, surface and thickness datasets for Antarctica. Cryosphere 7, 375-393. https://doi.org/10.5194/tc-7-375-2013.

Fricker, H. A., Padman, L., 2006. Ice shelf grounding zone structure from ICESat laser altimetry. Geophys. Res. Lett. 33 (15), L15502. https://doi.org/10.1029/2006GL026907.

Godin, O. A, Zabotin, N. A., 2016. Resonance vibrations of the Ross Ice Shelf and observations of persistent atmospheric waves. J. Geophys. Res. Space Phys. 121, 10157-10171. https://doi.org/10.1002/2016ja023226.

Griggs, J. A., Bamber, J. L., 2009. Ice shelf thickness over Larsen C, Antarctica, derived from satellite altimetry. Geophys. Res. Lett. 36, L19501. https://doi.org/10.1029/2009GL039527.

Holdsworth, G., 1969. Flexure of a floating ice tongue. J. Glaciol. 8 (54), 385 -397.

Ilyas, M., Meylan, M. H., Lamichhane, B., Bennetts L. G., 2018. Time-domain and modal response of ice shelves to wave forcing using the finite element method. J. Fluids Struct. 80, 113-131. https://doi.org/10.1016/j.jfluidstructs.2018.03.010.

Lee, H., Han, S., Han, H., 2018. Young's modulus of Antarctic ice shelves derived by double-differential interferometric *SAR*. EGU General Assembly 2018, Vienna, Austria.

Lescarmontier, L., Legrésy, B., Coleman, R., Perosanz, F., Mayet, C., Testut L., 2012. Vibrations of Mertz Glacier ice tongue, East Antarctica. J. Glaciol. 58 (10), 665-676. https://doi.org 10.3189/2012JoG11J089.

MacAyeal, D. R., Sergienko, O.V., Banwell, A. F., 2015. A model of viscoelastic ice-shelf flexure. J. Glaciol. 61(228), 635-645. https://doi.org 10.3189/2015JoG14J169.

Massom R. A., Scambos Th. A., Bennetts L. G., Reid Ph., Squire V.A., Stammerjohn S.E., 2018. Antarctic ice shelf disintegration triggered by sea ice loss and ocean swell, *Nature* 558, pages383–389.

Meylan, H. M., Bennetts, L. G., Hosking, R. G., Catt, E., 2017. On the calculation of normal modes of a coupled ice-shelf/sub-ice-shelf cavity system. J. Glaciol. 63 (240), 751-754. https://doi.org/10.1017/jog.2017.27.

Montiel F, Squire VA. 2017 Modelling wave-induced sea ice break-up in the marginal ice zone. Proc.R.Soc.A 473, 20170258. http://dx.doi.org/10.1098/rspa.2017.025.

Papathanasiou, T. K., Karperaki, A. E., Theotokoglou, E. E., Belibassakis, K. A., 2015. Hydroelastic analysis of ice shelves under long wave excitation. Nat. Hazards Earth Syst. Sci. 15(8), 1851–1857. https://doi.org/10.5194/nhess-15-1851-2015.

Papathanasiou, T. K., Karperaki, A. E., Theotokoglou, E. E., Belibassakis, K. A., 2014. A higher order FEM for time-domain hydroelastic analysis of large floating bodies in an inhomogeneous shallow water environment. Proc. Royal Soc. A, 471, 20140643. https://doi.org/10.1098/rspa.2014.0643.

Rabinovich, A. B., 2009. Seiches and harbour oscillations, in: Young, C. K. (Ed.), Handbook of Coastal and Ocean Engineering, Singapore, World Scientific. pp. 193-236.

Roach L.A., Smith M. M, Dean S.M. 2018, Quantifying Growth of Pancake Sea Ice Floes Using Images From Drifting Buoys, Journal Geophysical Research Oceans. https://doi.org/10.1002/2017JC013693.

Schulson, E. M., Duval P., 2009. Creep and Fracture of Ice. Cambridge University Press, Cambridge.

Sergienko O. V. 2017, Behavior of flexural gravity waves on ice shelves: Application to the Ross Ice Shelf J. Geophys. Res. Oceans, 122, 6147–6164, doi:10.1002/2017JC012947.

Sergienko, O. V., 2010. Elastic response of floating glacier ice to impact of long-period ocean waves. J. Geophys. Res. Earth Surf., 115 (F4), F04028, https://doi.org/10.1029/2010jf001721.

Sergienko, O.V., 2013. Normal modes of a coupled ice-shelf/sub-ice-shelf cavity system. J. Glaciol. 59 (213), 76–80. https://doi.org/10.3189/2013jog12j096.

Squire, V.A., Williams, T. D. 2008. Wave propagation across sea-ice thickness changes. Ocean Modell. 21, 1-11. https://doi.org/10.1016/j.ocemod.2007.10.006.

Sturova, I. V., 2007. Effect of ice cover on oscillations of fluid in a closed basin. Izv Atmosph. Ocean Phys. 43(1), 112-118.

Thomson, J., Ackley S., Shen, H. H., Rogers, W. E., 2017. The balance of ice, waves, and winds in the Arctic autumn. Eos, 98. https://doi.org/10.1029/2017eo066029.

Vaughan, D. G., 1995. Tidal flexure at ice shelf margins. J. Geophys. Res. Solid Earth, 100 (B4), 6213 - 6224. https://doi.org/10.1029/94jb02467.

Vinogradov, O.G., Holdsworth, G.H., 1985. Oscillation of a floating glacier tongue. Cold Reg. Sci. Technol. 10(3), 263–271.

Zhang, J., Schweiger, A., Steele M., Stern, H. 2015. Sea ice floe size distribution in the marginal ice zone: Theory and numerical experiments. J. Geophys. Res. Oceans 120 (5), 3484–3498. https://doi.org/10.1002/2015jc010770.